AFRL-RX-WP-TP-2010-4061

AN EXPERIMENTAL INVESTIGATION OF INTERMITTENT FLOW AND STRAIN BURST SCALING BEHAVIOR IN LiF CRYSTALS DURING MICROCOMPRESSION TESTING (Preprint)

D.M. Dimiduk, C. Woodward, and M.D. Uchic

Metals Branch
Metals, Ceramics, and Nondestructive Evaluation Division

E.M. Nadgorny

Michigan Technological University

P.A. Shade

UTC

JANUARY 2010
Interim Report

AIR FORCE RESEARCH LABORATORY
MATERIALS AND MANUFACTURING DIRECTORATE
WRIGHT-PATTERSON AIR FORCE BASE, OH 45433-7750
AIR FORCE MATERIEL COMMAND
UNITED STATES AIR FORCE

REPORT DOCUMENTATION PAGE

Form Approved
OMB No. 0704-0188

1. REPORT DATE *(DD-MM-YY)*	2. REPORT TYPE	3. DATES COVERED *(From - To)*
January 2010	Journal Article Preprint	01 January 2010 – 01 January 2010

4. TITLE AND SUBTITLE

AN EXPERIMENTAL INVESTIGATION OF INTERMITTENT FLOW AND STRAIN BURST SCALING BEHAVIOR IN LiF CRYSTALS DURING MICROCOMPRESSION TESTING (Preprint)

5a. CONTRACT NUMBER
IN HOUSE

5b. GRANT NUMBER

5c. PROGRAM ELEMENT NUMBER
62102F

6. AUTHOR(S)

D.M. Dimiduk, C. Woodward, and M.D. Uchic (Metals, Ceramics, and Nondestructive Evaluation Division, Metals Branch (AFRL/RXBM))
E.M. Nadgorny (Michigan Technological University)
P.A. Shade (UTC)

5d. PROJECT NUMBER
4347

5e. TASK NUMBER
RG

5f. WORK UNIT NUMBER
M02R1000

7. PERFORMING ORGANIZATION NAME(S) AND ADDRESS(ES)

Metals Branch (AFRL/RXBM)
Metals, Ceramics, and Nondestructive Evaluation Division
Materials and Manufacturing Directorate, Air Force Research Laboratory
Wright-Patterson Air Force Base, OH 45433-7750
Air Force Materiel Command, United States Air Force

Michigan Technological University

UTC

8. PERFORMING ORGANIZATION REPORT NUMBER
AFRL-RX-WP-TP-2010-4061

9. SPONSORING/MONITORING AGENCY NAME(S) AND ADDRESS(ES)

Air Force Research Laboratory
Materials and Manufacturing Directorate
Wright-Patterson Air Force Base, OH 45433-7750
Air Force Materiel Command
United States Air Force

10. SPONSORING/MONITORING AGENCY ACRONYM(S)
AFRL/RXLM

11. SPONSORING/MONITORING AGENCY REPORT NUMBER(S)
AFRL-RX-WP-TP-2010-4061

12. DISTRIBUTION/AVAILABILITY STATEMENT
Approved for public release; distribution unlimited.

13. SUPPLEMENTARY NOTES
PAO case number 88 ABW-2009-2952, cleared 30 June 2009. This work was funded in whole or in part by Department of the Air Force work unit M02R1000. The U.S. Government has for itself and others acting on its behalf an unlimited, paid-up, nonexclusive, irrevocable worldwide license to use, modify, reproduce, release, perform, display, or disclose the work by or on behalf of the U. S. Government. Submitted to Philosophical Magazine (Taylor & Frances).

14. ABSTRACT

Current research seeks methods for coarse graining the ensemble dislocation response. However, the physical understanding of intermittency micromechanisms is still lacking, thus limiting developments in this field. This paper reports on the first comprehensive experimental statistical study of plastic deformation of LiF microscopic samples having low initial dislocation densities, in both as-grown and gamma-irradiated conditions. The investigations used the microcompression testing method. Data sets were evaluated independently for the loading and flow deformation stages for each material. Investigations examined evolution of the strain-burst response in both the spatial and temporal domains. A new technique (described in detail) provided advances in quantitative evaluations of the statistical data relative to previous studies.

15. SUBJECT TERMS
coarse graining, micromechanisms, plastic deformation, LiF microscopic samples

16. SECURITY CLASSIFICATION OF:			17. LIMITATION OF ABSTRACT:	18. NUMBER OF PAGES	19a. NAME OF RESPONSIBLE PERSON (Monitor)
a. REPORT	b. ABSTRACT	c. THIS PAGE			Christopher F. Woodward
Unclassified	Unclassified	Unclassified	SAR	48	19b. TELEPHONE NUMBER *(Include Area Code)* N/A

Standard Form 298 (Rev. 8-98)
Prescribed by ANSI Std. Z39-18

Dennis M Dimiduk: dennis.dimiduk@wpafb.af.mil

An experimental investigation of intermittent flow and strain burst scaling behavior in LiF crystals during microcompression testing

D.M. DIMIDUK[1], E.M. NADGORNY[2], C. WOODWARD[1], M.D. UCHIC[1], P.A. SHADE[3]

[1] Air Force Research Laboratory, Materials and Manufacturing Directorate, Wright-Patterson AFB, OH 45433-7817, USA
[2] Michigan Technological University, Department of Physics, Houghton, MI 49931, USA
[3] UTC, Dayton, OH 45432, USA

Abstract

Current research seeks methods for coarse graining the ensemble dislocation response. However, the physical understanding of intermittency micromechanisms is still lacking, thus limiting developments in this field. This paper reports on the first comprehensive experimental statistical study of plastic deformation of LiF microscopic samples having low initial dislocation densities, in both as-grown and gamma-irradiated conditions. The investigations used the microcompression testing method. Data sets were evaluated independently for the loading and flow deformation stages for each material. Investigations examined evolution of the strain-burst response in both the spatial and temporal domains. A new technique (described in detail) provided advances in quantitative evaluations of the statistical data relative to previous studies. The findings showed that specimen-size-dependent strengthening might be tied to differences between dislocation nucleation and multiplication conditions. Platen displacement event cumulative probability distributions exhibited both Gaussian regimes at small displacements and power law regimes for event displacement, duration and average velocity at larger sizes. However, the observed event size scaling exponents did not follow the expectation from mean-field theory, revealing scaling exponents in the range from 1.9 – 2.8. Additionally, extraordinarily large displacements events were observed that exceeded the sizes of those found in previous studies by at least ten times. Quantitative clarification of the power-law exponent values and their dependence on deforming sample conditions demands both further experimental studies with larger numbers of samples and a wider range of sample conditions. Such studies would benefit from better matching of the time scales of dislocation processes and observation.

Keywords: size effects; microcompression; intermittency; scale-free flow; dislocation mechanisms

1. Introduction

Hirth and Lothe [1] begin their fundamental treatise on the theory of dislocations with the statement: “Probably the first suggestion of dislocations was provided by observations in the nineteenth century that the plastic deformation of metals proceeded by the formation of slip bands or slip packets, wherein one portion of a specimen sheared with respect to another.” Indeed, plastic deformation often occurs in a heterogeneous and intermittent manner at microscopic, mesoscopic and macroscopic levels (or in more general terms, as a result of dislocation nucleation, motion, multiplication, and interaction). Nonetheless, state-of-the-art simulation methods are hard-pressed to represent most aspects of these physical processes. While dislocation-dynamics methods currently reproduce selected aspects of the mechanisms of intermittency, they have yet to achieve a complete representation of mesoscale plasticity [2-9]. Present limitations on computational power, together with under-developed physics within the simulation codes (i.e. cross-slip, climb, crystal rotations and patterning to name a few), prevent realistic dislocation simulations over temporal and spatial domains that are readily accessible by experimental methods [9, 10]. Conversely, methods for simulating macroscopic plasticity rely upon flow rules and kinematical representations that intrinsically homogenize flow and strain hardening over all microscopic scales [11-13]. These disconnections between the known physical processes at various scales and the available simulation methods, suggest the need to better understand the physical mechanisms of intermittent flow and the ensemble behavior of dislocation structures. Such an understanding is needed so that the methods for coarse-graining the dislocation and strain hardening physics continue to advance.

Microcrystal compression testing was introduced in 2003 as a technique for experimentally studying microstructural effects in material deformation and is being applied to a growing variety of materials [14-19]. Regardless of crystal type, one characteristic feature associated with the dislocation properties of small crystals is an intermittent flow response in a form of strain bursts that dominates the nature of the flow curves [9, 15, 19-24]. This contemporary technique also allowed detailed experimental studies of selected statistical aspects of the strain-burst response in such metallic crystals as Ni, Al and Mo [20, 22, 24]. Those studies revealed a general scale-free power law relationship,

$$P(X) \propto X^{-\alpha} \tag{1}$$

between the probability density of strain burst events, *P(X)*, at a given burst size, *X*, that was determined by logarithmic binning and fitting of the burst events data. Specifically, for Ni microcrystals having diameters in the range from 20 to 30 μm, [20], found the relationship

$$P(X) \propto X^{-1.6\pm0.02} \tag{2}$$

using both logarithmic binning and analysis of the cumulative probability distributions (CPD). A power-law scaling exponent near to α ; 1.5 was commonly observed in all the prior studies—a value argued to be ‘universal’ and consistent with the mean-field theories [25-27]. A few studies considered why intermittency is such a characteristic feature of deformation at micrometer scales but not macroscopic scales and attempted to define the bounds on the features controlling the largest observed strain bursts [27-29]. Those studies argued that finite sample sizes lead to an exponential cutoff to the power law at large burst sizes leading to the relationship,

$$P(X) \propto X^{-\alpha} \exp[-\left(X/X_0\right)^2] \quad (3)$$

where X_o is the characteristic burst event size at large sizes (in the range from ~50 to ~230 nm [20, 28]). A similar relationship was also suggested within a framework of self-organized criticality (SOC) model with uncorrelated branching processes [30]. However, those studies draw inconsistent and perhaps incomplete conclusions, suggesting that the differing experimental methods and their relations to the behavior of particular materials are insufficiently grounded [27, 29]. The findings in turn suggest that it may be premature to draw conclusions about the appropriate coarse-graining framework for mesoscopic deformation simulations until the underlying dislocation physics governing each selected testing method are better understood.

At the same time, micrometer-scale sample deformation investigations of different crystals seems to be a good method for studying those new aspects of dislocation physics on the microscopic (i.e. nucleation and motion of single dislocations having nanometer-scale characteristics) and mesoscopic levels (i.e. formation of dislocation dynamical arrays, slip lines and glide bands having larger than nanometer characteristic scales). Therefore, the present paper addresses selected aspects of intermittent flow during microcompression testing. Based on a prior study [21], the effort focuses on LiF crystal in two different forms and for a range of microcrystal sizes. LiF offers numerous distinct advantages for such fundamental investigations, among which are its ready availability in an ultrapure form having an extremely low initial dislocation density, as described in detail later. Additionally, experimental methods permit easy introduction of point defect populations into the crystals via irradiation. Thus, the dislocation dynamical response can be compared for materials having rather different inherent critical resolved shear stresses and thermally activated dislocation responses. This study presents the first analysis results regarding the characteristics of intermittency in LiF microcrystals. In so doing, the study uses a newly applied technique for examining the experimental data and determining power-law parameters associated with specimen displacement bursts. The results are discussed relative to selected topics associated with microcrystal experiments and observations of strain burst behavior in other materials and by techniques.

2. Microcompression experiments, materials, test specimens and analysis methods

Since the findings in this study come about via the new microcompression technique and new methods for analyzing data, more detailed descriptions of these topics are given in this section. Section 2.1 briefly describes the materials used for the study and the general attributes of the microcompression stress-strain curves and deformed specimens. Section 2.2 expands the description of selected testing details that affect interpretation of flow intermittency. Lastly, Section 2.3 describes the analysis methods used to explore micromechanisms of specimen behavior and intermittency.

2.1. Microcompression of LiF materials

The microcompression technique is described in numerous publications and remains the subject of an expanding suite of investigations [16, 19]. The essence of the method is to form micrometer-scale columnar single crystals in relief on an oriented surface of bulk sample material (usually a single crystal or large grain-size specimens). Since the isolated columns

remain attached to the bulk crystal at one end, the sample may be readily positioned for deformation within a microscale testing machine. The most common practice involves isolation of columnar specimens via focused ion beam machining and, performing mechanical deformation using the highly sensitive and precise nanoindentation systems that are widely available as commercially supplied instruments [19]. Those methods were employed for testing samples during the present study.

Single crystal LiF is representative of alkali halide (AH) ionic crystals having the sodium chloride structure that are among the most widely studied materials regarding dislocation dynamics [1], as summarized in Section 4.1. These crystals are often referred to as having the rock salt structure, an ordered derivative of the face-centered cubic (FCC) structure. The structure consists of two interpenetrating FCC lattices, one for each type of ion in the compound [31]. Bulk ultrapure (< a few ppm total impurities) LiF single crystals of good structural perfection with an extremely low dislocation density ($<10^9$ m^{-2}) are available commercially. Annealing the crystals can further reduce the dislocation density. Oriented samples for mechanical testing can be easily prepared by cleavage along {100} planes. Finally, the damaged outer layer of a sample can be easily removed, for instance by chemical polishing [32].

The magnitude of the Burgers vector in LiF, $b = <110> a_0/2 = 0.285$ nm, where a_0 is the lattice spacing, is the smallest among AH materials. Plastic deformation of such AH crystals occurs by glide in the primary glide system $<110>\{1\bar{1}0\}$. There are also two secondary glide systems, $<110>\{001\}$ and $<110>\{\bar{1}11\}$ [32]. Accordingly, during plastic deformation of a sample having the <001> compression axis, the axial displacement corresponding to a single Burgers vector shear is $\delta L_{\min} = b/\sqrt{2} = 0.2015$ nm.

Two high purity bulk LiF single crystals (Saint-Gobain Crystals, OH, USA) were obtained for this study, each having total impurity content less than several ppm. One of the crystals was irradiated by a ^{60}Co gamma-source (radiation energy of ~1 MeV) while the other was left in the 'as-grown' condition. The resultant radiation defect concentrations are unknown but the crystal was yellow colored and considerably hardened after irradiation [21]. This indicates a high concentration of γ-radiation induced defects that can considerably reduce the dislocation mobility and increase the yield and flow stresses. Such defects are typically predominantly small clusters of halogen interstitials in AH crystals γ-irradiated at room temperature [33]. Compression tests were performed on <001>-oriented parallelepiped samples having dimensions roughly equal to 3 x 3 x 8 mm to assess the properties of both types of bulk LiF crystals. When examined by selective etching, the average initial dislocation density for both the as-grown and irradiated crystals was observed to be $\rho_o < 10^9$ m^{-2}. Separately, samples having 1, 5, and 20 μm diameters oriented for microcompression along <001> were prepared from bulk crystals using either an FEI Strata DB235 or Nova Nanolab FIB-SEM with a FIB accelerating voltage of 30kV [16]. Multiple samples were prepared at each of the sizes and, scanning electron microscope images were used to measure the sample dimensions prior to testing. Microcompression testing was performed using a modified MTS NanoXP nanoindentor outfitted with a diamond flat punch tip. Additional details regarding these microsamples and their mechanical behavior are reported elsewhere [21].

A report describing the room temperature stress-strain behavior of the specific LiF samples investigated in this study of intermittency was published previously [21]. Figure 1 shows selected examples of the stress-strain curves (a and b) and the corresponding measured

microcrystal flow stress ranges shown on a dislocation velocity – stress plot (c). Johnston and Gilman obtained the dislocation velocity data shown in Figure 1c from the first fundamental study of bulk LiF [33]. SEM images of deformed microcrystals corresponding to some of the stress-strain curves of Figure 1 are shown in Figure 2. Notable regarding these tests is the use of a so called "hybrid" testing method that achieves real-time switching of the testing device control mode depending upon sample flow conditions. The implications of this on data analysis are described in the following two subsections.

Intermittent flow of microcompression specimens was also studied previously for Ni, Al and Mo crystals [20, 22, 24]. The first two of those studies provide power-law relationships for the probability of strain burst events at a given burst size where the strain burst size was defined via a platen displacement or velocity condition persisting above some constant threshold (*Th*) value for a time interval [20, 22]. While drawing slightly different conclusions, both studies noted selected practical uncertainties associated with optimizing the signal-to-noise ratio for displacement data analysis (window averaging of data records) and selecting the value of the threshold constant used to identify events. Noting the recent study by Clauset et al., that treats the general question of how to find power-law relationships within data, the present study employed a revised method for optimizing the window averaging of the data, setting the threshold level and numerically fitting the power law relationship [34]. The new method is described in the following within the context of the present microcompression testing study.

2.2. Experimental technique and test data

For the microcompression test, recorded 'raw primary data' consists of the current elapsed time, *t*, the platen position, *L(t)*, and the applied load, *P(t)*. Typically, one computes stress on the sample, $\sigma(t)$, incremental or difference displacement, $\delta L(t) = L(t)_2 - L(t)_1$ (or platen velocity, $V(t) = \delta L / \delta t$), total strain, $\varepsilon(t)$, and stress rate, $\delta\sigma/\delta t$. Selectively, these may be used to affect the test control within a closed loop. For the present tests, the nanoindentor was operated at a control frequency of 10 kHz, while the aforementioned data were recorded at 50 Hz. The testing conditions specified a constant programmed platen velocity, V_p, in the range from 0.2 to 4.4 nm/s, depending upon the sample height, so as to maintain a nominal initial strain rate of $\delta\varepsilon_e / \delta t + \delta\varepsilon_p / \delta t = \delta\varepsilon / \delta t = 10^{-4}\ \mathrm{s}^{-1}$, where ε_e, ε_p, and ε are the elastic strain, plastic strain, and total strain, respectively.

However, during the test dislocation motion proceeds as bursts of glide area swept during which the dislocation velocity is expected to exceed V_p by many orders of magnitude (perhaps 10^5 - 10^7 greater than V_p) and, for the microcrystal sample $\delta\varepsilon_p/\delta t >> 10^{-4}\ \mathrm{s}^{-1}$ during those intervals. For the hybrid test method, detected sample displacement bursts prompt the control algorithm to change from an 'active loading' ($\delta\sigma/\delta t >> 0$) to a constant stress hold or 'creep' regime ($\delta\sigma/\delta t \approx 0$), so as to maintain force (a constant far-field driving force) on the sample through to the natural cessation of the burst. The stress hold continues until such time when V_p multiplied by the test elapsed time Δt nearly corresponds to the current platen position, i.e. the conditional $\varepsilon_p + \varepsilon_e < \Delta t \left(\delta\varepsilon / \delta t \right)$ being satisfied triggers a stress increase once again. Such changes in specimen displacement rate lead to shifts in the average displacement rate over the duration of the test.

Both the shifting average specimen displacement rate and the controlled repeated changes from loading, to creep and back to loading again, suggest that applying a constant single threshold to the testing data may be inappropriate. A constant threshold artificially truncates and segments (or extends and groups, depending upon specific testing conditions) the strain bursts, especially those that initiated under loading control and continuing into the creep portions of the test, even though the far-field driving force remained unchanged.

Further, the incremental-displacement versus time record $\delta L(t)$ inevitably contains numerous small variations at or near to the expected programmed displacement, as may be deduced from the loading rate. Window averaging the $\delta L(t)$ record dampens the variable signal and enhances the 'signal-to-noise'; however, selecting the size of the window for averaging, w, remains a heuristic process [22]. Further, while studies heretofore and present treat those small fluctuations as 'noise' [20, 22], later discussion of the results from this study provides physical motivation for a more thorough analysis of all studies at some future time.

Thus, in order to examine these many detailed features associated with microcompression testing data, each recorded data set was separated into two sets for 'loading' (L) and 'flow' (F) stages. The $\delta\sigma/\delta t$ (incremental stress rate) values were examined to approximately determine the first extended stress hold after the $\delta\sigma/\delta t$ maximum that inevitably occurred at the proportional limit stress. The records occurring before that stress-hold are considered the loading set and those after are the flow set. Thus, the aforementioned data analysis was carried out on 4 data sets; as-grown (AG) loading (AGL) and flow (AGF), irradiated (IR) loading (IRL) and flow (IRF) and, for three sample sizes, 1, 5 and 20 μm, within each set.

2.3. Data analysis methods

The present analysis method was designed to provide better insights in the selection of values of the averaging window, w (an integer number of successive data records), for data analysis. Further, the method varied the value of the threshold parameter, $Th(t)$, according to both the instantaneous condition of testing control and a systematic variation for the current value of w.

To better illustrate the method, Figure 3 shows a typical cumulative probability distribution (CPD) for all the data records obtained for a test (a) and a histogram for the noise signal observed for a test (b), both after smoothing for $w = 5$ data records. Note that this CPD contains the measured incremental platen displacement records $\delta L(t)$ and, no threshold has yet been applied (as discussed previously) to determine strain burst event sizes, X. Figure 3b also shows the histogram for raw data before smoothing, and those the qualitative features apply to all tested samples. Viewing Figure 3a from left to right it is apparent that measured incremental test displacements exhibit a non-power law, high probability of occurrence, small-displacement regime that blends seamlessly into power-law like, less frequently occurring larger-displacement regime, as shown by the dashed line that was obtained by the optimization methods described later. The result indicates that no inherent features associated with the incremental displacement distributions readily separate the two regimes, thus prompting the use of optimization methods to seek the lower size limit of power law intermittency behavior. The histograms of Figure 3b are plotted from binned values of $\delta L(t)$ for values of $\delta L \leq 0.2$ nm, without regard to the loading or creep conditions. The signal fluctuations near to the nominal programmed displacement increment per recorded data point, $\delta L_p = 0.088$ nm, reasonably adhere to a Gaussian response as indicated by the fit lines for the measured and $w = 5$ records. The fit lines were determined using

only the bin sizes below 0.11 nm, but are plotted over the full displayed range of bin sizes (Figure 3b).

Both mean, M, and mean plus one standard deviation, $M + S$, values for the averaged data are also shown in Figure. 3b. The value of $M = 0.0867$ nm for the averaged fit, corresponds well to the value of δL_p for this test. By comparing the number of observed δL values to the Gaussian fit line, one sees that the number of incremental displacements begins to exceed the Gaussian expectation for $\delta L > M + S$. In a previous study, such information was evaluated and a fixed threshold value of $Th = M + 2S$ was selected for analysis [20]. For the present study the Th value was permitted to vary over a range both below and well above the $M + S$ value. A more detailed consideration of effects of small events on the statistical data analysis will be presented later.

Considering the hybrid testing method, the $\delta L(t)$ record for each test was divided into regions of loading and creep by evaluating the value of the stress rate $\delta\sigma/\delta t$ at each time record and comparing it to a value slightly above $\delta\sigma/\delta t = 0$. The loading and creep portions of the data were examined separately to find time intervals Δt_l and Δt_c over which no strain bursts were judged to occur and the value of M closely adhered to the programmed displacement ($\delta L_p = 0$ for creep, $\delta L_p = V_p \delta t$ for loading). For the selected Δt_l and Δt_c intervals, the mean and standard deviation values M_l, S_l, M_c and S_c, respectively, were solved. As the value of w was systematically varied during analysis, the values of M_l, S_l, M_c and S_c were re-evaluated over these same Δt_l and Δt_c intervals. Finally, to calculate the platen displacement burst event sizes, X_i, various multiples of S_l and S_c, selected to define the corresponding thresholds, as

$$Th_l = M_l + nS_l \tag{4_1}$$

$$Th_c = M_c + nS_c \tag{4_2}$$

where n is a real number multiple that scales the threshold value and is normalized to the standard deviation. Here, these displacement bursts, X_i, were defined as the total displacement, $X_i = \Delta L_i$ over a time interval Δt_i (the burst duration) for which successive values of $\delta L_i > Th$, where $Th = Th_l$ or Th_c for loading and creep regimes, respectively. Note that the value of Th changed during bursts events as they were frequently initiated during loading and continued then ended during creep conditions. Figure 4 shows an example portion plot of the $\sigma(t)$ and $\delta L(t)$ record, with and without averaging, along with the M and Th values for the same region of data. As seen, the averaging appreciably reduces raw data scattering, both during the loading and creep regimes.

For statistical data suspected to follow power laws (in this case the sets of X_i values), Clauset, et al., [34] demonstrate that large errors may be present when power-law parameters are deduced by linear regression of probability density (the method that was used in nearly all prior studies of dislocation burst motion behavior). Finding the smallest event size, $X_i = X_{min}$, above which the power law is a good fit to the data, presents particular problems, yet that value has a strong influence on the deduced exponent. Clauset, et al., recommend an iterative procedure of fitting the data whereby the scaling exponent α is given by the 'maximum likelihood estimator' (MLE),

$$\alpha = 1 + N\left[\sum_{i=1}^{N} \ln \frac{X_i}{X_{\min}}\right] \tag{5}$$

where N is the total number of events. Such a procedure iteratively employs the MLE to find power-law fit parameters to cumulative probability distributions of experimental X_i values, $S(X)$; generates an ideal model distribution, $P(X)$, using those fit parameters; quantitatively compares the two and, continues the procedure until a goodness-of-fit parameter is converged. To test the goodness of fit, Clauset et al., recommend using the Kolmogorov-Smirnov (KS) statistic parameter, D, that quantifies the distance between the fit and the ideal model probability distributions [34]. The optimization goal is to select X_{min} to minimize D, the maximum difference between those cumulative distribution functions given as

$$D = \max_{X_i \geq X_{\min}} \left| S(X) - P(X) \right| \tag{6}$$

where $S(X)$ and $P(X)$ are the fit and ideal model cumulative probability distributions, respectively. Thus, for any set of X_i, the optimal value of X_{min} (and thus α) is the value that minimizes D. Clauset, et al., go on to recommend procedures for testing the power-law hypothesis for the data; however, those procedures have not been implemented for the present study.

To achieve a systematic evaluation and definition of the platen displacement event data (X_i), a matrix was selected for values of averaging window size and threshold (w and n in Eqn. 4) over which the measured data (δL_i) were examined. Typically, that matrix consisted of varying w as an integer from 1 – 9, and n in increments of 0.2 from 0.0 – 3.4. The same value of n was used for both the loading and creep regimes for any values of w and n. MATLAB codes were written to find Th_l and Th_c values and for each element of the $w \times n$ matrix to process the $\delta L(t)$ record and find the corresponding set of X_i values, accordingly. Further, using the recommendations and selected MATLAB codes described in [34] and provided by Clauset, et al. at their Internet site, optimized power-law fit parameters were obtained for the data from each tested microsample. Contour plots were constructed to show the variations in these parameters with values of w and n. Figure 5 shows examples of the fit parameter contour plots, including the power-law exponent (α, Figure 5a), KS statistic (D, Figure 5b), lower power-law cutoff (X_{min}, Figure 5c), maximum-size event (X_{max}, Figure 5d), and total number of events detected (N, Figure 5e). Note that while each value of w and n yield a set of X_i having corresponding optimal values of α, D, etc., those values alone do not indicate the optimal choice for w and n for the given sample or for groups of combined samples. Thus, for each sample, similar plots were examined and 'best choice' values of w and n were selected giving progressively decreasing priority the following criteria: i) a low sensitivity of α to w and n, ii) a relatively low value of D, iii) a value of N away from the relative peak for low values of w and n, iv) low values of X_{min} and, v) relatively unchanging values of X_{max}. To the extent possible, efforts were made to use a common value of w and n for grouping samples within a common category; i.e. all 5 μm samples within the flow region would have common 'best choice' values. With few exceptions, values of $w = 4$ and $n =$ 0.7 to 1.5 were selected.

To better illustrate the influence of the small platen-displacement events, it is useful to examine the effect of changes to the values of w and n on fitting the optimized power law for a single sample. Figure 5f shows the CPD constructed for a constant number of total events, counting from the largest event to the 679th event. The CPD are prepared for four different selections for w and n for a single 5 μm AGF sample. Inspection of Figure 5f reveals that for

small values of w and large values of n, the cumulative probability of X_i smaller than ~0.4 nm decreases as does the largest event size, relative to the other selections shown in the figure. For the $w = 1$ condition and a high value of n (which mimics the prior study of Ni microcrystals [20], the largest platen-displacement events are separated into smaller events. As the values of w increase to 3 or 4 and the value of n is selected for optimal values of D as may be deduced from Figure 5b, the X_{min} parameter decreases and the CPD of event sizes shifts to larger values of X_i. Still further increases in the value of w may begin to average away the smallest increments of $\delta L(t)$ and artificially increase the size of intermediate X_i values, thus again decreasing the probability of small X_i and adding convex curvature to the shape of CPD. Changes to these parameters affect the value of α in turn. By comparing the CPD in Figure 5f to ones shown later in Figures 6b and 7b, one may observe that an individual sample may or may not accurately reflect the population of larger displacement events. Thus, it may be important to collectively consider a broad set of individual sample responses, as well as the collective set of combined responses, both within the context of the w and n sampling space, to find the most consistent or robust power law for the sample set.

After selecting values of w and n for grouped repeat sample sets, the corresponding sets of X_i values were selected and combined with other sets to form populations of X_i for common sample sizes, stages of the flow curve and material type (see below). For those populations the values of α, D, X_{min}, and X_{max} were re-optimized and are reported in the remainder of this paper. Similar procedures were also used for these combined populations to find the cumulative probability distributions and power law characteristics for burst event durations, Δt_i, and event average velocity, $V_i = X_i/\Delta t_i$

As a validation of the codes and methods, selected samples from the Ni microcrystals previously studied and reported by Dimiduk, et al., [20] were re-analyzed using the current method. Values of α ranged from 1.38 to 1.75 via the new method, while values ranging from 1.53 to 1.67 were originally reported. The current method also detected a larger number of events for each sample. Those findings will be reported elsewhere.

3. Results

The findings from this study are described in the next two sections. A synopsis of the stress-strain curves and sample appearance results were provided previously in Section 2.1 and Figures 1 and 2. Consequently, Section 3.1 describes the strain-burst platen-displacement statistics via fit cumulative probability distributions (CPD) along with other distinguishing features. Following that, Section 3.2 presents the observed temporal aspects of the platen-displacement statistics.

3.1. Platen displacement event power laws

Figure 6a-c compares the fit X_i CPD for the two materials and two deformation stages of each material, at a constant specimen size, for the aggregated samples tested at each condition. For each part of the figure, solid lines are shown that indicate the range of the optimized power law fits to the four data sets. Beside each line a corresponding value for the power law slope, α, that was determined via Equations (1) and (2) is also shown. The 20, 5 and 1 μm samples are grouped within Figures 6a-c, respectively. Note that displacement events exceeding ~1000 nm

in a single event occurred for both 5 and 20 μm diameter samples. The largest observed events of X_i = 3156 nm for a 20 μm and X_i = 1117 nm for a 5 μm IRF samples correspond to very large single-burst engineering strains of ~6.3 and 8.8 %, respectively. The specific power-law fit exponents for each data set are provided in Table I, together with minimum and maximum values of X_i determined via the optimization routines. While space limitations prevent showing a detailed comparison of the power-law fits to each CPD data set, inspection of those fits revealed the sensitivity of the fit to X_i events at small sizes, near to the transition to Gaussian-like response. Table I shows a qualitative trend toward rising X_{min} values with a decreasing number of samples (also decreasing N not shown), suggesting a possible influence of sparse data sets in some cases. One may also note from Table I that the displacement sensitivity of the instrument, together with the data analysis procedures, yield displacement information (X_{min} values) corresponding to platen motions substantially smaller than a unit Burgers vector shear displacement (< 0.2 nm) that correspond to power-law behavior. On the other hand, for selected data sets the detected X_{min} values are ~7 times larger.

To examine the influence of sample diameter (and correspondingly applied stress), the CPD were re-grouped by flow stage and these may be compared in Figure 7a-d. Figures 7a and 7b show the CPD for the AGL and IRL data sets, respectively. Both of these show the trend that the value of α increases with decreasing sample diameter. These sets also show that the population of event sizes tends to shift to smaller sizes for smaller diameter samples. By comparing the CPD shown previously in Figure 5f to ones shown in Figures 6b and 7b, one may observe that an individual sample may or may not accurately reflect the population of larger displacement events.

To gain insight into the 'typical' sizes of the large strain events (those contributing the most plastic strain) occurring for the varying materials and sample sizes, Figure 8a shows the AGF data set CPD re-plotted using only the largest 3563 events for each sample size, while Figure 8b shows similar CPD using the largest 2764 events for each sample size of IRF data. For each plot, the total number of detected events for the least populous data set determined the number of events to be used in the comparisons.

3.2. Temporal aspects of platen displacement

While the complete platen displacement and velocity records as a function of stress and time could not be included because of space limitations, Figure 9 shows examples of the platen displacement and velocity as a function of time for two cases of samples having completely different temporal behavior but with seemingly similar stress-strain diagrams (although at different stress levels, see corresponding data in Figure 1). Even these two examples can illustrate complex intermittent behavior of dislocation ensembles in deforming microsamples as measured by the platen motion. The diagrams show small displacement events (velocity spikes) during the loading stages, transitions to the flow stage and a long Stage I deformation period. However, as seen from Figure 9b an extremely large displacement and rather high platen velocity have occurred at the very beginning of the transition to the flow stage for sample IR 5 μm #4, unlike sample AG 1 μm #2 shown in Figure 9a. Note also the different scales for the platen velocity in the two cases. As a rule, such samples also demonstrate a rather complicated shape after deformation as shown previously by the corresponding sample images in Figure 2.

To evaluate the platen-displacement events in the time domain the strain burst event data were evaluated to find the event durations, Δt_i, and event average platen velocity, V_i. For every

set of X_i, the starting and ending times were determined for each event. Using that information, the duration for each event was determined and, dividing the event size by the event duration derived the average platen velocity over the event. Thus, Figure 10a-d shows plots of X_i versus Δt_i for the 1, 5 and 20 μm diameter samples for each material type and loading stage. Each plot shows a fit line for the 20 μm sample data. The plots reveal that for both materials and all deformation stages most of the events occur in the size–duration space near to the fit line, the slope of which indicates a population average velocity, V_s of ~1 nm/s (see fit values indicated on Figure 10). The plots also show that the loading stages have a slightly higher value of V_s than the flow stages. Finally, further inspection of the plots indicates that many events extend to X_i values that far exceed the population-average expectation given their duration. Such events must have values of V_i in excess of V_s.

While not specifically shown by separate figures, the CPD for event durations were found to exhibit power law regimes of the type

$$P(\Delta t_i) \propto \Delta t_i^{-\tau} \tag{7}$$

where τ is the event duration scaling exponent. Table II shows a summary of the event durations for the same sample sets shown in Table I.

A more detailed view of the average platen event velocity is shown in Figures 11 and 12. The fit V_i CPD for the two materials and two deformation stages of each material, at a constant specimen size, are shown in Figure 11, while the V_i CPD for various specimen sizes at a constant deformation stage and material type are shown in Figure 12. As revealed by Figures 11 and 12, the event average velocity also exhibited power law regimes given by

$$P(V_i) \propto V_i^{-\nu} \tag{8}$$

where ν is event average velocity scaling exponent. Value ranges for ν are shown by the bounding lines along side of the data plotted in Figure 12.

As an initial evaluation of the time correlations that may exist between platen displacement events, the values of X_i, Δt_i and V_i were plotted as a function of the event starting times, for each material type, deformation stage and sample diameter. Selected example plots of these data are shown in Figure 13.

To further evaluate platen-displacement event scaling, the $\delta L(t)$ records were examined for single specimens over time intervals corresponding to a single X_i event. Those records provided information about the event shapes that could be compared within single specimens for changing magnitudes of X_i. Examples of these are shown in Figures 14-15.

4. Discussion

Since as mentioned before, LiF is one of the best-studied materials regarding dislocation dynamics and mechanical properties at the macro-scale, the features of bulk-crystal LiF deformation are first considered in some detail in Section 4.1 to establish a foundation for interpreting the remainder results. Section 4.2 discusses selected additional aspects of the microcrystal stress-strain results relative to bulk crystal behavior. Following that, Section 4.3

treats the platen displacement power law statistics in the context of current literature on intermittency and strain bursts. Finally, Section 4.4 offers selected perspectives regarding the temporal behavior of microcrystal displacement and intermittency.

4.1. Dislocation behavior of bulk-crystal LiF

Since the pioneering study of dislocation velocities, density evolution and plastic flow of bulk LiF by Johnston and Gilman [33], numerous similar studies of dislocation dynamics in LiF and other AH crystals have confirmed and refined their findings (see for instance reviews [31, 32]). The most important feature of plastic deformation in bulk LiF crystals is temporal and spatial intermittency of the shear strain progressing through coordinated dynamical sequences of moving single dislocations, dislocation dynamical arrays, narrow slip lines, widening glide bands, and transition from single to multiple slip. In turn, each series of such events corresponds to different (and usually spatially distinct) instances of dislocation nucleation and multiplication. Additionally, when deformed by compression, the crystals can take different final shapes depending upon the relative contributions from each of the events in the series on the available slip planes. Importantly, a similar series of deformation events are also observed during microcompression of LiF microsamples [21].

4.1.1. Basic principles of dislocation intermittency

It is well known that a dislocation ensemble resulting from dislocation motion and multiplication during plastic deformation has irreversible time-dependent and non-equilibrium properties. Under the applied stress, a single dislocation can move in a jerky manner and without multiplication as demonstrated by *in-situ* deformation inside an electron microscope. Hence, even a small group of such dislocations moving with velocity v would produce strain bursts but only rather small ones. Larger bursts occur after multiplication increases the number of moving dislocations in the ensemble. Such dislocations dissipate energy into the deforming crystal at a rate of Bv^2, where B is the dislocation drag coefficient. When the applied stress is kept constant, the dislocation ensemble relaxes and eventually can reach an equilibrium state. Of course, *spontaneous microscopic fluctuations* (i.e. bursts) should also exist at equilibrium but one may expect that they are relatively small and Gaussian-like, as is typical of equilibrium systems. Thus, when a Gaussian response occurs, such as the one observed in the present experiments, it is not necessarily associated with experimental or extrinsic noise. Rather, it is a natural state for the dynamical system from which evolution proceeds.

When under increasing applied stresses, the dislocation ensemble is removed from equilibrium as stress increments force the dislocations to move and multiply producing strain bursts that disturb the ensemble. Such a non-equilibrium ensemble starts returning back to equilibrium, via a series of dislocation (strain) bursts, as soon as the external stress ceases to increase. Since the dislocation velocity in a majority of crystals is a strongly non-linear function of stress, similar to those shown in Figure 1c for LiF, a standard linear response theory cannot be applied to the dislocation ensembles. Hence such “non-equilibrium” bursts are expected to be different than spontaneous fluctuations, i.e. not necessary small and Gaussian. The first direct measurements of dislocation bursts in Ni and LiF microsamples support this general conclusion: bursts were found to be in a wide range of sizes, from very small to rather large, micrometer sizes, and follow the power law relationship [20, 21].

Another general question concerning the dislocation ensembles and their fluctuations/bursts is what kind of intermittency they can exhibit. Their properties indicate that they cannot be described as Gaussian random quantities resulting from the sum of many random numbers. Rather, the bursts should be governed by the so-called intermittent random quantities of the multiplication type, which are products of a large number of independent random quantities [35]. Such multiplicative random quantities typically appear in the solution of evolving stochastic systems. For additive Gaussian quantities the relative fluctuation strength does not grow with time, while the multiplicative intermittent random quantities produce fluctuations that grow with time. This latter case corresponds to the case of the intermittent shear strain rate in deforming micrometer-scale samples, described through the swept-area rate of dislocations loops and segments bowing out between obstacle landscapes always present in real materials.

This general description gives a brief account of the principles of dislocation ensemble dynamics not only in LiF but also in other deforming materials. As seen, the microcompression technique used in this study exactly follows the above description: indeed, temporal intermittency having a scale-free platen displacement response has been observed in the study of Ni, Al and Mo microsamples as previously mentioned [20, 22, 24].

4.1.2. Formation of dynamical arrays and their conversion into multiplying slip lines

The first observable motion of existing single dislocations in deforming bulk LiF samples starts well before the pronounced yield stress, σ_y. As usually revealed by selective dislocation etching, the dislocations are moving rather slow (Figure 1c) and without multiplication at such low stresses. When the applied stress rises, small groups of moving dislocations loops and lines form the so-called *dynamical arrays* [1, p. 781]. They appear at applied stresses close to the elastic limit stress $\sigma \geq \sigma_e$ and are nucleated by surface and bulk stress-concentrator-type dislocation heterogeneous sources, such as sample edges, surface microsteps, inclusions or precipitates [36, 37]. The dynamical arrays move initially without multiplication and resemble inverse pileups, with a rather small number of sparse, widely spaced dislocations and the smallest spacing near the sources. Since the velocity of the edge-character dislocations v_e in LiF is higher than that of screw-character dislocations, v_s, dislocation loops and lines are comprised of long predominantly screw-character single dislocations of the same sense. Experiments show that the dislocations at the head of each dynamical array move considerably faster than an individual single dislocation, sometimes by several orders of magnitude [38]. In present-day terminology, these first arrays forming in a bulk sample are the "intermittent events" or "dislocation avalanches." Their "size," (corresponding axial displacement) can be estimated as $N\delta L_{\min} = N\,b/\sqrt{2}$, which is ~20 nm for a typical number of $N \approx 100$ dislocations, which correspond to a rather small strain of ~10^{-6} that would normally be undetected in a macroscopic compression test. Although the stress is high enough for nucleation of dislocations at local stress concentrators, the applied stress that leads to the first dislocation motion and array formation is still below a critical stress required for multiplication of dislocations by double cross-slip. Double cross slip is the main mechanism that generates new dislocations and edge-character dipoles in LiF [37] and other AH crystals [31, 32].

The leading dislocations in the dynamical arrays obey the same velocity-stress dependencies $v(\sigma)$ as single isolated dislocations shown in Figure 1c [38]. The corresponding velocity-stress

dependencies at a constant temperature can be described by power laws having rather high and low exponents of ~20 and ~1, respectively for the low stress and higher stress regimes [33]. The dislocation velocities in these two ranges also have quite different temperature dependencies indicating the different nature of the crystal resistances to dislocation motion for those ranges. It should be noted that such dependencies are typical not only of LiF and other AH crystals but also many metallic single crystals. This provides support for a view that such a steep rise in the dislocation velocity under a relatively small change in local stress is one of the reasons for the observed intermittency in dislocation ensembles. The dislocation velocity at $v > 1$ m/s follows a relationship of $v = \sigma b / B$, where B is the dislocation drag coefficient per dislocation unit length.

Since the displacement of each dislocation emerging at the surface of the deforming sample produces a slip step with a height of $b/\sqrt{2}$, such slip steps allow further analysis of dynamical arrays development. Indeed, if N dislocations of the same sense in a moving dislocation group cross the same point on the surface, they create a higher step of $Nb/\sqrt{2}$. However, if new dislocation semi-loops appear inside the group due to double cross-slip, the height of some of such slip steps would be smaller since the semi-loop has ends of opposite sense and the 'negative' end subtracts from the slip-step height. Using selective etching to reveal each dislocation position in the group and surface topography technique (such as optical interferometry [39]) for the profile measurements, one can follow the evolution of a dynamical array from the very beginning till its conversion into the multiplying array that is usually called the *slip line* or narrow glide band.

Such an analysis indicates that the newly formed dynamical arrays move without multiplication and that each such array is composed of screw-character dislocations of the same sense, i.e. the dislocations nucleated from a single concentrator-type source. By the time the applied stresses approaches the yield stress, roughly 200 dislocations or thereabouts have been nucleated in each array. The slip step heights of new dislocations that appeared later cease to increase: instead, the slip step heights start reducing indicating active multiplication by double cross-slip [39]. Almost simultaneously, one observes widening of the slip lines in the lateral direction that also confirms the action of double cross slip process [33, 40]. This marks the beginning of Stage I where the applied stress is either constant or only slightly increases indicating easy glide pattern with preferential single slip. It is in this stage that the slip lines begin conversion into widening *glide bands*.

4.1.3. Nucleation distance and further evolution of slip lines

The same experimental techniques [39] also allow measuring the distances between the new multiplied dislocations to calculate the average nucleation distance Λ. The experimental average nucleation distance in bulk pure LiF crystals can be as large as $\Lambda \approx 1$ mm but can be much less in crystals with higher yield stresses [40]. As experiments show, the measured localized shear strain provided by the motion of those nucleated dislocations in the slip lines strongly depends on the stress level. However, if the sample size is $< \Lambda$, the strain is considerably reduced indicating a decrease in the number of new dislocations and their average density [40]. Additional experiments reveal that the nucleation distance Λ becomes shorter in LiF crystals with higher yield stresses, regardless of the reason, be it doping, irradiation, lower test temperature, or higher strain rate. All of such special features can be attributed to the stochastic nature of double cross slip.

Indeed, a phenomenological model suggested by Wiedersich [41] and confirmed by numerous experiments in LiF and other AH crystals [40], suggests that the multiplication process depends on two geometrical parameters, the length *l* of the dislocation segment available for cross-slip and distances *h* of cross slip, both of which are random quantities. The former controls initiation of double cross slip, similar to Frank-Read (FR) source action. However, unlike FR sources the degree of multiplication by double cross slip is also governed by the distance *h*. Depending upon the magnitude of *h* and the appropriateness of the interaction between the cross-slipped and non-cross-slipped segments, there are three possible results: i) a new dislocation loop is produced if distance *h* is large enough; ii) trails of vacancies are generated if *h* is less than several atomic spacings; iii) finally, edge dipoles are created in case of intermediate *h*. Consequently, the new dislocation density increases as the local stress becomes higher since more and shorter cross-slipped segments are able to multiply, including edge dipoles that can act as both main obstacles to dislocation motion and dislocation sources. This means that the nucleation distance Λ decreases as the applied stress is raised. Note that for a given slip line, the number of leading dislocations that move without multiplication is kept approximately constant, $N \approx 200$, independent of the sample's yield stress. At the same time, these dislocations are distributed over a distance close to the corresponding nucleation distance. These findings have allowed us to introduce the size-limited dislocation generation (SLDG) concept that can explain aspects of the stress-size dependence observed in micrometer-scale samples of different materials [21]. This concept is directly related to the "starvation" concept in present-day terminology [18] and, likely governs a large part of the present-day descriptions of the "exhaustion" regime [9, 19, 42]. A detailed description of the SLDG model and its application to micron-scale samples will be presented elsewhere.

Since the dislocations in a slip line move with rather high velocities at $\sigma \geq \sigma_y$, the slip lines reach the opposite surface of the sample soon after the beginning of the easy glide stage, and the distribution and density of dislocations in slip lines almost cease further changing. This is because the density of dislocations and edge dipoles become rather high, thus contributing to a stronger resistance to further dislocation motion inside the slip lines. It is believed that the appearance of immobile edge dipoles, created by the double cross slip mechanism, are responsible for the corresponding higher resistance to dislocation motion in Stage I [40]. During this stage, the previously narrow slip lines are gradually converted into wider glide bands where newly-multiplied dislocations can move easily in the dislocation-free bulk volume only near the band edges. Eventually, the average dislocation velocity becomes lower when more such wide glide bands overlap, so that a higher applied stress is needed to provide the same dislocation flux.

The onset of glide band interaction and overlap marks the beginning of a higher strain-hardening rate in Stage II where the other three secondary slip systems in LiF become active [43]. However, the easy glide stage is seldom if ever observed in samples having a high density of surface micro- or macroscopic defects. For such cases different slip systems are randomly activated in various parts of such samples leading to local hardening with a fast transition to Stage II. It is interesting to note that in LiF the hardening rates in Stages I and II are almost the same as those in FCC Ni.

4.2. Microsamples and stress-strain diagrams

Several common features typical of micron-size LiF compression samples can be seen from stress-strain diagrams shown in Figure 1a and Figure 1b. Perhaps the most striking is the close

similarity of these stress-strain curves with those obtained from metallic microcrystals [19]. For instance, even though the yield stress of AG bulk LiF is lower than that of pure Ni by a factor of ~35, the flow stresses are almost the same in the microcrystals of corresponding sizes. Additionally, the distinctive characteristics of the pre-yield loading (or quasi-elastic) stages and plastic flow stages are in close agreement in these microcrystals [21]. Thus, based on phenomenology alone one can expect that the main underlying mechanisms are also similar although not in all quantitative details.

As discussed previously elsewhere [21], the increase of the applied stress (microcrystal strengthening) in the loading stage is one of the main features of all microcrystals. The stage is not totally elastic as revealed by 'plasticity pop-ins' or small strain bursts observed throughout the loading stage. Such slip events first appear as short steps in the stress-strain curve at stress levels not much higher than the macroscopic yield stress and become longer and more visible as the applied stress rises. They are especially pronounced during loading of smaller samples, as clearly seen for all 1 μm sample loading curves, but are typical of the loading stage for microsamples of all sizes. The extremely low initial dislocation density in the LiF crystals used in this study tends to exclude the option that the pop-in slip events appear as a result of motion of existing dislocations. Rather, new dislocations are likely nucleating and moving from surface microdefects that serve as stress concentration dislocation sources, similar to macroscopic LiF deforming samples described previously in Sec. 4.1. Recent computer simulations of dislocation heterogeneous nucleation by such sources also confirm this conclusion [44]. Also, the pop-in events may be associated with single-arm source operation on a slip trace, which is an alternate form of local dislocation nucleation that could lead to equivalent strains [9]. However, in either case the fact that pop-in slip events are spatially distinct, isolated at dynamical arrays as revealed by SEM examination, and separated in time by increasing elastic loading, indicates that these strain bursts are unable to produce a sustainable dislocation flux or mass multiplication. As seen in Figure 1, the resulted loading stage exhibits intermittent strain bursts over a stress range that spans from a low intrinsic elastic limit stress to extremely high stresses as the sample sizes are reduced to 1 μm in diameter.

There is however a principal difference between bulk and micron-scale samples in the loading stage. First, in bulk crystals the newly nucleated dislocations move relatively slowly because the stresses are quite low as may be deduced from the data shown in Figure 1c. As a surface source nucleates more dislocations in those crystals, they all continue to move inside the bulk sample until they start to multiply after traversing an average nucleation distance. The distance is much shorter than a typical size of a bulk sample but the yield point is marked when dislocations on average traverse the nucleation distance. On the other hand, in LiF microcrystals of a low initial dislocation density with the sample size << Λ, the first dislocations nucleated by a surface source may leave the sample or in rare cases interact with debris (exhaust) before multiplication [9]. Additionally, as the stress level builds up to higher values, the dislocation velocity also increases according to Figure 1c. The first pop-in strain bursts are displayed in the stress-strain diagram as a result of such non-multiplying strain events.

As mentioned above in Section 4.1, the average nucleation distance Λ decreases as the stresses increase, and that attribute is common to many materials [31, 33, 40, 45]. In a sense, this fact justifies a self-consistent mechanism of the size dependence of the flow stress in all microsamples. Indeed, as soon as the stresses in the loading stage are high enough so that the distance Λ becomes close to the sample diameter D, the conditions for double cross slip multiplication are satisfied for all subsequent dislocation nucleation. Their multiplication,

together with the corresponding increase in the mobile dislocation density ρ and the high dislocation velocity v, lead to such an increase in the product $b\rho v$ that it ends up close to the programmed strain rate. As a result, the loading stage transforms into the flow stage.

Selected SEM images of the deformed AG and IR samples were shown in Figure 2. The first image of AG 5-μm sample #4 (where compression stopped at $\varepsilon = 3.2$ % and $\sigma_{max} = 216$ MPa) shows single slip in the primary slip system developed in the upper part of the sample. Higher compression strains can activate secondary orthogonal slip system and two oblique slip systems, as in IR 5 μm sample #1 ($\varepsilon_{max} = 8.6$ % and $\sigma_{max} = 200$ MPa) or in IR 1 μm sample #3 ($\varepsilon_{max} = 9.5$ % and $\sigma_{max} = 660$ MPa). The 1 μm samples for both material types demonstrate the largest slip off-sets and localization to narrow slip bands/traces. Further compression over $\varepsilon > 20\%$ creates more complicatedly shaped samples. When the dislocation density increases with deformation, the orthogonal systems become predominant since the mutual crossing of oblique systems is more difficult than activation of orthogonal systems as a result of differences in latent hardening [40]. In such cases samples take a form of a barrel due to restricted slip near the platen, as in IR 20 μm sample #3 ($\varepsilon_{max} \sim 21.0$ % and $\sigma_{max} = 120$ MPa), or of a distorted barrel with well-developed slip zones, as in AG 5 μm sample #2 ($\varepsilon_{max} = 23.8$ % and $\sigma_{max} = 247$ MPa). The most complicated shape is observed when all four possible slip systems are activated. Two pairs of slip systems are developed having orthogonal orientations but occurring separately in the upper and lower halves of the sample, rotated by 90 degrees relative one another, as in AG 20-μm sample #2 ($\varepsilon_{max} = 21$ % and $\sigma_{max} = 140$ MPa) and IR 5 μm sample #4 ($\varepsilon_{max} \sim 25.1$ % and $\sigma_{max} = 210$ MPa).

4.3. Displacement event power law scaling

From the previous descriptions of Figures 3 – 5 and Table I and, the analysis methods used for this study, one may glean that the analysis of the data is uncertain despite the use of computerized optimization tools for the power law fit. The principal source of the uncertainty in the displacement domain is the result of the seamless transition from the expected Gaussian response of the ensemble dynamics at small displacements to a scale-free response for larger events. The very largest events have virtually no effect on the power law exponent since their occurrences are so infrequent. While this leads to uncertainty in the lower limit of scale-free response and the power law exponent, the existence of a scale free regime is unequivocal.

The plots of Figure 6 and summary listed in Table I reveal at least three new features relative to prior reports of power laws and scale-free flow for dislocation plasticity. First, the scaling exponents consistently exceed (beyond uncertainty) the nominal value of $\alpha = 1.6$ mentioned previously and described in other studies, irrespective of the deformation stage or sample size. Second, the CPD tend to group by deformation stage rather than material type, for each sample size, although the relative values of α change for the two stages (loading and flow) as a function of sample size. For example, in Figure 6a for the 20 μm samples, the CPD for the AGF and IRF data tend toward the limiting slope of $\alpha = 2.65$ (greater than for the AGL and IRL stages), while for the 1 μm samples shown in Figure 6c, those same flow-stage CPD tend toward the lower limiting slope of $\alpha = 2.00$, now lower than that for the loading stage results. Third, the 20 μm IRF, 5 μm AGF and IRF, and 1 μm AGL CPD, each exhibit a trend toward large-size platen-displacement events that, while relatively infrequent, are more frequent than the power law expectation (CPD turns upward at large X_i). For example, Figures 6a and 6b show that values

X_i > 100 nm occur about 2 – 4 times more frequently for the IRF 5 and 20 μm samples than for the same sample sizes in AGF material and condition. Further, such large events were not observed for the loading stage. However, the other data sets exhibit either the nominal power law expectation, or an event probability less than the power law trend at large event sizes (CPD turns downward, perhaps from a finite size cut-off). Interestingly, for the AGL cases there are no clear differences in the observed largest event size with changing sample diameter, even though the corresponding strains at a fixed event size significantly vary with sample diameter.

For the AGF and IRF stage results, such trends with sample diameter are less clear. In general, the event CPD cluster over a tighter range of event sizes between 0.1 and 100 nm, independent of sample diameter (Figures 6 and 7). However, that trend for the data is not necessarily reflected in the fit values of the power law exponents as indicated by the solid lines. This feature clearly emphasizes that the population of the small events has a significant influence on the optimized fit power law and emphasizes the need to remove subjectivity from the analysis methods. Thus, for platen displacement events greater than ~1 nm, there is much less spread in the CPD for the flow regime than for the loading regime, even though that difference may not be reflected in the fit scaling exponent. A slightly different view of these results may be obtained by comparing the CPD for a fixed number of events for each sample in the comparison as was shown in Figure 8. These comparisons show a systematic change in the CPD toward smaller event sizes for smaller samples and for most cases a decreasing power law exponent accompanies the change (see Table I).

4.4. Displacement temporal scaling

For the most part, the results regarding temporal scaling for all aspects of the study are affected by the fact that the instrument data collection frequency (perhaps together with platen inertia) is far too low to directly record the dislocation events in real time, thus presenting challenges for interpreting the results. These same challenges most likely influence all other studies of dislocation bursts via direct strain measurements. For example, from Figure 1a and b, one can estimate how many dislocations are moving during such pop-in events. Given an axial platen displacement per one dislocation as ~0.2 nm in LiF (as the smallest event) and a large pop-in event size, for instance in a 1 μm sample of about 0.2 – 0.3%, such bursts correspond to only a small number of dislocations, between one and about 20-40 dislocations. Secondly, since the applied stress in the deforming microsamples increases in the loading stage, the dislocation velocity also increases even in 20 μm samples and can be >> 1 m/s (Figure 1c). Conservative estimates then give ~20 μs for the time necessary for the dislocations to travel over a 20 μm sample and only ~1 ns over a 1 μm sample. Since the recorded time steps of the experiment are much longer, 0.02 s for data recorded frequency of 50 Hz in this study, and because of inertia of the platen, those “extreme” bursts cannot be recorded individually but are combined into larger pop-in events. Such behavior and instrumentation limitations also apply in the flow stage where multiplication is the main source of new dislocations, translating into much larger intermittent platen displacements. Thus, conservative estimates suggest that dislocation motion occurs on time scales of ns - μs, while the data recording time interval is 0.02 s in this study. Accordingly, for these types of experiments, while position or displacement resolution is at the scale of single dislocation movements, the microcompression system temporal resolution is many orders of magnitude slower than the expected real scale of dislocation dynamics. Thus, one may speculate

that it would be interesting for a future study to observe the changes to the strain burst population for much higher data recording frequencies.

Nonetheless, selected general conclusions may be drawn relative to the temporal domain for intermittency. Figures 9 and 10 suggest that while a vast majority of strain burst events exhibit sizes that are proportional to their duration (exhibit constant ensemble velocity), the largest events deviate from that trend for all loading material types, deformation stages and sample sizes. These may lead to extremely large events that, as shown by Figure 15, occur with fluctuating platen velocity over the duration of the event. Also, from Table II one may observe that the duration scaling exponent, τ (Eqn. (7)), tends to rise with decreasing sample size while the maximum event duration decreases. These findings indicate that either a stress-dependence to the event durations occurs, perhaps by stress-induced nucleation and entanglement of dislocations that limits events, or the physical dimensions over which dislocation slip may be active limit those event durations.

Figures 11 and 12 both show that the trends for event average velocity are mostly determined by sample size, which implies applied-stress dependence to the platen event velocity distribution. Figure 11 shows the CPD qualitatively span a similar range of V_i values, irrespective of the loading stage or material type. Alternatively, Figure 12 shows that CPD of V_i values separate by sample size for a selected loading stage or material type. Further inspection of Figure 12 also indicates that CPD qualitatively separate into two regimes. At low V_i (below ~10 nm/s for 20 μm samples or ~4 nm/s for 1 and 5 mm samples), the cumulative probability $>V_i$ drops sharply. However, a second regime appears to exist for large values of V_i and that regime shows power law scaling where the scaling exponent ν (Eqn. (8)) varies in the range from 2.0 to 3.7. For the AGL and AGF data, the power law scaling extends over more than one order of magnitude for both the 1 and 5 μm samples; however, that scaling regime does not appear to be present for the larger 20 μm diameter samples. For the IRL and IRF materials, the power law regime begins to develop for the loading stage for all sample diameters but is most pronounced for the 1 and 5 μm samples in the flow regime for which it extends over more than two orders of magnitude.

Inspection of the plots in Figure 13 reveals that a vertical line-like pattern develops, especially for the flow regime data. Such patterning indicates that events are correlated with each other in time indicating a true shock and aftershock or avalanche-type behavior. As a trend, such plots for the flow stage indicate that the magnitude of X_i trends toward smaller values as the test progresses in time and that event activity occurs as clusters in time separated by intervals of only small (<1 nm) events (see Figures 13b, c). More detailed evaluations of the event correlations will be the subject of a separate report.

Finally, considering the platen-event shapes shown in Figures 14 and 15, three types of shapes were found that may be qualitatively described as i) 'square-wave' like (Figure 14), ii) irregular 'saw-tooth wave'-like (Figure 15a) and, iii) 'spike-saw-wave' like (Figure 15b). Figure 14 shows the square wave-like events for a 1 μm diameter AGF sample. Note that the events exhibit the property of affine scaling over two orders of magnitude. Such square-wave like events were found for both deformation stages and materials for small sample diameters. Figure 15a shows the irregular saw-wave type events that were typically found for 20 μm diameter samples during both deformation stages and for both materials. The 20 μm AGL example shown suggests that single platen-displacement events X_i consist of an integrated set of highly irregular platen motion fluctuations δL_i over a time interval. To a first order, those fluctuations also exhibit affine scaling of their magnitudes and durations. The third type of event shape was only associated with the largest observed events (greater than ~70 nm) in both material types during

the flow stage. Figure 15b shows examples of this type of event occurring within a 5 μm diameter specimen of AGF material. This type of events (the largest events) inevitably consisted of a large characteristic displacement occurring near to the beginning of the event followed a succession of saw-tooth-like displacements of lesser magnitude occurring over the remaining time interval of the event.

5. Summary and conclusions

The new testing, recording and analyzing techniques as described in detail in this paper allow us to obtain more reliable and quantitative information about deformation events in micron-scale LiF single crystals of high structural perfection. This new combined data treatment method reveals new stochastic features of dislocation dynamics not available before and applicable to future studies. Almost 30 samples of three sizes, 20, 5 and 1 μm oriented for single slip, were fabricated from two types of bulk LiF crystals, as-grown and gamma irradiated, that are representative of a wide class of ionic AH crystals having the rock salt structure. Both bulk crystals have practically identical, extremely low initial dislocation density and concentration of impurities but considerably different yield stress because of the irradiation. Based on these investigations, we draw the following conclusions:

1. The measured experimental data for LiF materials validate the conclusions of the previous investigations of metallic single-phase materials, such as FCC (Ni, Cu, Al, Au) and BCC (Mo), regarding the size effects in plastic deformation. Namely, the qualitative microsample behavior is similar in all crystals studied so far, regardless of their crystal structure, bonding type, dislocation type, initial dislocation density and impurity concentration [19]. The only exception to this result so far may be the preliminary studies on Ti alloys [42].
2. Separate examination of two data sets for each sample as done in this study reveals an extended loading (or pre-yielding) stage and a flow (large strain burst) stage, indicating a conceptual difference between the two stages. A mixture of primarily elastic and plastic deformation is observed in the loading stage, where successive pop-in strain bursts occur, likely due to newly nucleated dislocations moving from surface dislocation sources. However, those plastic events cannot sustain general plastic deformation because at their occurrence, the local stresses do not support double cross slip dislocation multiplication in crystals of these sizes. Accordingly, so long as the sample size is smaller than the stress-dependent nucleation distance, the multiplication probability is rather low, preventing flow.
3. As a result, increased elastic deformation follows each pop-in until the applied stress is high enough to decrease the nucleation distance to a value closer to the sample dimensions, hence initiating massive dislocation multiplication and a transition to the flow stage. One of the advantages of our samples is that stress-dependence of the nucleation distance has been confirmed experimentally in LiF justifying this conclusion about the nature of the size effect. The same conclusion is probably valid also for Ni micron-scale samples, where quite similar differences between the loading and flow stages have been also observed.

4. The measured cumulative probability distribution of platen displacements within the range of the smallest detected events is not necessary a scale-free CPD but is closer to a Gaussian distribution (or rather to a mix of the Gaussian and some component of the scale-free regimes). On the other hand, the analysis of the entire strain-event range corroborates the previous findings of power law relationships. In terms of data recording, better time resolution is needed to unravel the dislocation contributions to the small-event range. The larger event range, on the other hand, is characterized by clear intermittent scale-free patterns in all studied samples: both the platen displacement data and platen temporal (duration and velocity) data follow power law scaling.
5. However, the scaling exponents for platen displacement in the power-law regime are found to be between 1.9 - 2.8 depending upon the crystal type, sample size, and deformation stage. These values are significantly greater than 1.5 - 1.6, the often reported exponents of the event size scaling obtained from computer simulation, mean-field theory and some experimental studies of dislocation dynamics. Such exponent values also indicate a possible violation of the "universality principle" in plastic deformation of microsamples despite their power law behavior, although a smaller exponent value of about 1.5 is often believed to be an intrinsic, universal property of all the critical, scale-free systems.
6. Another unexpected finding is the occurrence of very large strain-bursts, at least an order of magnitude greater than previously reported for any material. This finding corroborates the emerging notion of genuine scale invariance and intermittency of dislocation bursts in deforming solids.
7. The largest strain bursts nearly always occur early in the flow stage soon after the transition from the loading stage and are always significantly greater, sometimes by more than 100:1, than those in the loading stage. They occur at the unique period of deformation when dislocations readily multiply at high stress relative to sample size, but the overall density is extremely low. That finding alone supports the notion of dislocation interactions (strain hardening) being a control mechanism limiting burst size throughout the subsequent deformation stages.
8. Quantitative clarification of the power-law exponent values and their dependence on deforming sample conditions demands both further experimental studies with larger numbers of samples and a wider range of sample conditions (i.e. initial dislocation density, source types, etc). Such studies would also benefit from further improvements to the statistical analysis tools and computational materials models. Finally, they would also benefit from better matching of the time scales of dislocation processes and observation.

Acknowledgment

The authors have been supported by the Air Force Research Laboratory and the Air Force Office of Scientific Research. PAS also acknowledges support from the AFRL/RX Science and Technology for the 21st Century Program. The authors also thank T.A Parthasarathy, S.I. Rao, and R. LeSar for numerous technical discussions during the course of this work. Finally, the

authors gratefully acknowledge the work by Clauset et al., described in reference [34] below and thank them for making selected MATLAB analysis codes available for public use.

References

[1] J.P. Hirth and J. Lothe, *Theory of Dislocations* (Krieger, Malabar, 1992)
[2] B. Devincre, L. Kubin, C. Lemarch and R. Madec, . Mater. Sci. Eng. A 309-310 (2001) p.211.
[3] K.W. Schwarz, J. Appl. Phys. 85 (1999) p.108.
[4] M. Tang , M. Fivel and L.P. Kubin, Mater. Sci. Eng. A 309–310 (2001) p.256.
[5] C. Motz, D. Weygand, J. Senger et al., Acta Mater. 57 (2009) p.1744.
[6] T. Ohashi, M. Kawamukai, H. Zbib, Inter. Jol. Plast. 23 (2007) p.897.
[7] N.M. Ghoniem, S.H. Tong and L.Z. Sun, Phys. Rev. B 61 (2000) p.913.
[8] D.M. Dimiduk, M.D. Uchic, S.I. Rao et al., Model. Simul. Mater. Sci. Eng. 15 (2007) p.135.
[9] S.I. Rao, D.M. Dimiduk, T.A. Parthasarathy et al., Acta Mater. 56 (2008) p.3245.
[10] D.M. Dimiduk, M. Koslowsky and R. LeSar, Scripta Mater. 54 (2006) p.701.
[11] R.J. Asaro, J. Appl. Mech. 50 (1983) p.921.
[12] A. Needleman, Acta Mater. 48 (2000) p.48.
[13] L. Kubin, T. Hoc and B. Devincre, Acta Mater. 57 (2009) p.2567.
[14] M.D. Uchic, D.M. Dimiduk, J.N. Florando and W.D. Nix, Proc. Symp. MRS 753 (2003) p.1.
[15] M.D. Uchic, D.M. Dimiduk, J.N. Florando, W.D. Nix, Science 305 (2004) p.986.
[16] M.D. Uchic, D.M. Dimiduk, Mater. Sci. Eng. A 400-401 (2005) p.268.
[17] D.M. Dimiduk, M.D. Uchic and T.A. Parthasarathy, Acta Mater. 53 (2005) p.4065.
[18] J.R. Greer, W.C. Oliver and W.D. Nix, Acta Mater. 53 (2005) p.1821.
[19] M.D. Uchic, P.A. Shade and D.M. Dimiduk, Ann. Rev. Mater. Res. (2009) (In press).
[20] D.M. Dimiduk, C. Woodward, R. LeSar and M.D. Uchic, Science 312 (2006) p.1188.
[21] E.M. Nadgorny, D.M. Dimiduk and M.D. Uchic, Proc. Symp. MRS 976E (2007) p.EE06-24; J. Mater. Res. 23 (2008) p.2829.
[22] M. Zaiser, J. Schwerdtfeger, A.S. Schneider *et al.*, Phil. Mag. 88 (2008) p.3861.
[23] A.S. Schneider, B.G. Clark, C.P. Frick et al., Mater. Sci. Eng. A 508 (2009) p.241.
[24] K.S. Ng and A.H.W. Ngan, Acta Mater. 56 (2008) p.1712.
[25] M. Zaiser and P. Moretti, J. Stat. Mech. P08004 (2005).
[26] M. Zaiser, Adv. Phys. 55 (2006) p.185.
[27] M. Zaiser and N. Nikitas, J. Stat. Mech. P04013 (2007).
[28] F.F. Csikor, Ch. Motz, D. Weygand *et al*., Science 318 (2007) p.25.
[29] J. Weiss, T. Richeton, F. Louchet et al., Phys. Rev. B 76 (2008) p.22411022.
[30] K. Christensen and N.R. Moloney, *Complexity and Criticality*, ICP, London, 2005, p.270.
[31] M.T. Sprackling, *The Plastic Deformation of Simple Ionic Crystals*, Academic Press, London, 1976.
[32] E.M. Nadgornyi, *Dislocation Dynamics and Mechanical Properties of Crystals*, J.W. Christian, P. Haasen and T.B. Massalski eds., Pergamon Press, Oxford, 1988.
[33] W.G. Johnston and J.J. Gilman, J. Appl. Phys. 30 (1959) p.129.
[34] A. Clauset, C.R. Shalizi and M.E.J. Newman, arXiv:0706.1062v2 [physics.data-an], 2009.

[35] Ya.B. Zeldovich, A.A. Ruzmaikin and D.D. Sokoloff, *The Almighty Chance*, World Scientific, Singapore, 1990.
[36] J.J. Gilman, J. Appl. Phys. 30 (1959) p.1584.
[37] W.G. Johnston and J.J. Gilman, J. Appl. Phys. 31 (1960) p.632.
[38] S.I. Zaitsev and E.M. Nadgornyi, Sov. Phys. Solid State 12 (1970) p.1468.
[39] B.I. Smirnov, Sov. Phys. Solid State 9 (1967) p.319.
[40] B.I. Smirnov, *Dislocation Structure and Crystal Hardening*, Nauka, Moscow, 1981.
[41] H. Wiedersich, J. Appl. Phys. 33 (1962) p.854.
[42] D.M. Norfleet, PhD thesis, The Ohio State University, 2007.
[43] E.M. Nadgornyi and B.I. Smirnov, Sov. Phys. Solid State 8 (1967) p.1628.
[44] D.E. Segal, C.Li and G. Xu, Phil. Mag. 86 (2006) p.5083.
[45] A.S. Argon and E. Orowan, Phil. Mag. 9 (1964) p.1003.

Figure Captions

Figure 1. Selected examples of the stress-strain diagrams of AG and IR LiF of 20-, 5-, and 1-μm samples (a, b), and corresponding flow stress ranges shown on a dislocation velocity–stress plot (c). In (c), IR 1, 2, and 3 stand for neutron irradiation flux of $2.3x10^{13}$, $2.3x10^{14}$, and $2.3x10^{15}$ n/cm^2, respectively.

Figure 2. SEM images of selected deformed samples, for which flow diagrams are shown in Figure 1. Note the dramatic differences in the sample shapes. Also note that two sides of the sample are shown for the IR 20 μm #3 sample.

Figure 3. (a) A typical cumulative probability distribution for incremental platen displacement (δL) illustrating separation of Gaussian and power-law distributions for small and large events. The dashed line is a power law fit to the date. The lower limit of the power fit was found using the optimization methods described in the text. (b) Histograms for a sample showing details of the "noise" signal (raw and smoothed data) for small $\delta L < 0.2$ nm.

Figure 4. Plot of a 35 s time interval of combined data records showing stress-time dependence $\sigma(t)$ (continuous line) and difference displacement-time dependence $\delta L(t)$ (different points for raw data and after averaging over 5 time records ($w = 5$). Note the different adjustment values of threshold parameters during loading and creep stages, Th_l and Th_c, respectively.

Figure 5. Example contour plots, in window-multiple, w - n, coordinates; (a-e) for AGF 5-μm sample #2. Similar plots are used for all studied samples to optimize five parameters, the scaling exponent α (a), Kolmogorov-Smirnov statistic parameter D (b), the smallest X_{min} (c) and largest X_{max} (d) event sizes, and (e) the total number of events, N. Such plots were examined and compared to select values for w and n to obtain the best-fit event size distribution $P(X_i)$ (f), as suggested by Clauset *et al*. [34]. Note that X_{min} and X_{max} are optimization parameters relative to a presumed power law and not the real measured smallest and largest events. Also note changes to the distribution $P(X_i)$ in (f) for different sets of the paired values w-n.

Figure 6. Optimized event size cumulative probability distributions $P(X_i)$ obtained from four different data sets, AGL, AGF, IRL, and IRF, and grouped for samples of the same diameter, 20 μm (a), 5 μm (b) and 1 μm (c).

Figure 7. The same cumulative probability distributions $P(X_i)$ from the same data sets as in Figure 6 but re-grouped according to the loading (a, c) and flow (b, d) stages in AG (a, b) and IR (b, d) samples, to demonstrate the size effect.

Figure 8. Event size cumulative probability distributions for the largest events from the AGF (a) and IRF (b) data sets illustrating the sample size effect.

Figure 9. Examples of the platen position $L(t)$ (solid lines) and velocity $\delta L(t)/\delta t$ (dots) for a typical (a) and extreme case (b) demonstrating significantly different temporal intermittency patterns, a smooth transition from the loading stage with many pop-in events into flow stages in (a) and a sharp transition from the loading stage with almost no pop-in events into flow stages in (b) (see Figure 1). Inset in (a) shows higher resolution view of a short time interval. Note the change in platen velocity scale in (a) between primary plot (log scale) and inset (linear scale). Also note ~6x change in platen displacement scale between the two plots.

Figure 10. Dependence of the event size X_i as a function of the event duration Δt for AGL (a), AGF (b), IRL (c), and IRF (d) data sets of 20-μm, 5-μm and 1-μm samples. The platen velocities averaged over all sizes are also given. Note the practically equal population average velocity in all cases.

Figure 11. Platen velocity distributions $P(V_i)$ obtained from four different data sets, AGL, AGF, IRL, and IRF, and grouped for samples of the same diameter, 20 μm (a), 5 μm (b) and 1 μm (c).

Figure 12. The same distributions $P(V_i)$ from the same data sets as in Figure 11 but re-grouped according to the loading (a, c) and flow (b, d) stages in AG (a, b) and IR (b, d) samples, to demonstrate the sample size effect.

Figure 13. Examples of development of temporal patterns in irradiated 20-μm and 5-μm samples: the events size X_i as a function of the event start time t of IRL (a) and IRF (b, c) data sets. Note the intermittent event patterns in all three plots; changes in the pattern between the loading and flow stages (a, b) and between two samples in the flow stage (b, c). The plots may be compared to the corresponding stress-strain curves and post deformation sample SEM images in Figures 1 and 2, respectively.

Figure 14. Four examples of platen incremental displacement $\delta L(t)$ taking the form of square wave-like pulses over the time interval of a single event. Each plot corresponds to one event integrated X_i event in the same deforming AG 1-μm sample during the flow stage. Note a change in scale for $\delta L(t)$ in each plot demonstrating self-affine scaling over almost two orders of magnitude.

Figure 15. Two examples of platen incremental displacement $\delta L(t)$ as a function of time over single event duration taking on a more complex form akin to small, irregular “saw tooth” wave-like pulses from AGL 20-μm data set (a) and larger, decaying “spike saw” wave-like pulses from AGF 5-μm data set (b). Note the much longer platen oscillations and motion durations than those shown in Figure 14.

Table I. Statistical Analysis Results for Event Size from LiF Sample Aggregates

Sample Set	Alpha*	Min Event Size	Max Event Size
AGL 20 µm	2.07 (3)	0.86 nm	46.7 nm
AGL 5µm	1.94 (4)	0.37 nm	37.9 nm
AGL 1µm	2.45 (4)	0.09 nm	28.4 nm
AGF 20 µm	2.65 (2)	1.39 nm	147.7 nm
AGF 5 µm	2.21 (4)	0.27 nm	1075.4 nm
AGF 1 µm	2.00 (4)	0.15 nm	56.0 nm
IRL 20 µm	2.00 (2)	0.83 nm	95.4 nm
IRL 5 µm	2.38 (6)	0.21 nm	9.97 nm
IRL 1 µm	2.77 (4)	0.24 nm	8.83 nm
IRF 20 µm	2.27 (2)	1.08 nm	3155.6 nm
IRF 5 µm	2.13 (5)	0.22 nm	1116.7 nm
IRF 1 µm	2.33 (4)	0.10 nm	51.6 nm

* Numbers in parenthesis indicate total number of samples at the indicated condition.

Table II. Statistical Analysis Results for Event Durations from LiF Sample Aggregates

Sample Set	Tau*	Min Event Duration	Max Event Duration
AGL 20 µm	2.57 (3)	0.48 s	6.62 s
AGL 5µm	4.11 (4)	0.20 s	0.68 s
AGL 1µm	8.61 (4)	0.20 s	0.28 s
AGF 20 µm	2.68 (2)	0.60 s	11.8 s
AGF 5 µm	2.80 (4)	0.48 s	19.8 s
AGF 1 µm	3.55 (4)	0.98 s	7.3 s
IRL 20 µm	2.40 (2)	0.34 s	10.1 s
IRL 5 µm	4.14 (6)	0.20 s	0.82 s
IRL 1 µm	4.11 (4)	0.26 s	0.66 s
IRF 20 µm	2.41 (2)	0.36 s	19.1 s
IRF 5 µm	2.76 (5)	0.54 s	21.1 s
IRF 1 µm	3.19 (4)	0.34 s	1.40 s

* Numbers in parenthesis indicate total number of samples at the indicated condition.

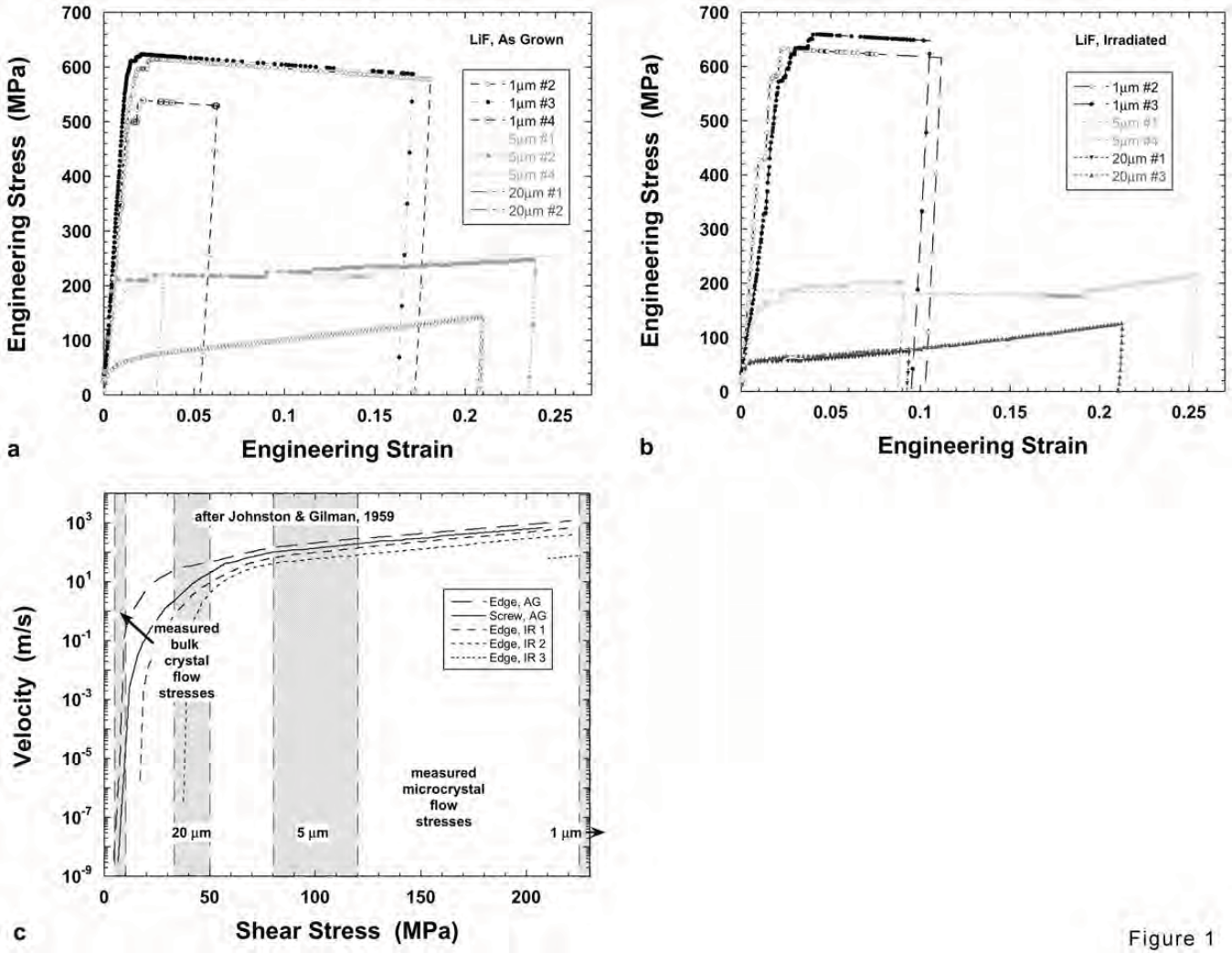
LiF, As Grown
1μm #2
1μm #3
1μm #4
5μm #1
5μm #2
5μm #4
20μm #1
20μm #2
Engineering Stress (MPa)
Engineering Strain
a
LiF, Irradiated
1μm #2
1μm #3
5μm #1
5μm #4
20μm #1
20μm #3
Engineering Stress (MPa)
Engineering Strain
b
after Johnston & Gilman, 1959
Edge, AG
Screw, AG
Edge, IR 1
Edge, IR 2
Edge, IR 3
measured bulk crystal flow stresses
measured microcrystal flow stresses
20 μm
5 μm
1 μm
Velocity (m/s)
Shear Stress (MPa)
c

Figure 1

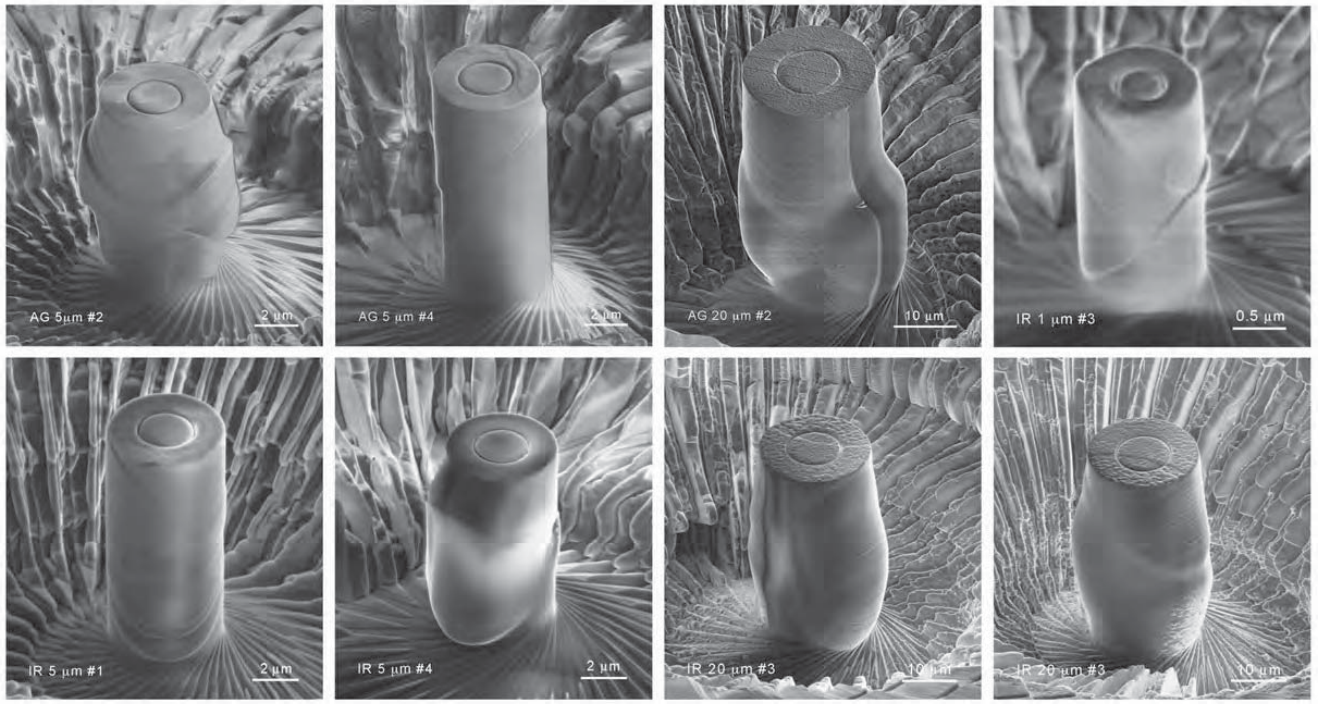
AG 5μm #2
2 μm
AG 5 μm #4
2 μm
AG 20 μm #2
10 μm
IR 1 μm #3
0.5 μm
IR 5 μm #1
2 μm
IR 5 μm #4
2 μm
IR 20 μm #3
10 μm
IR 20 μm #3
10 μm

Figure 2

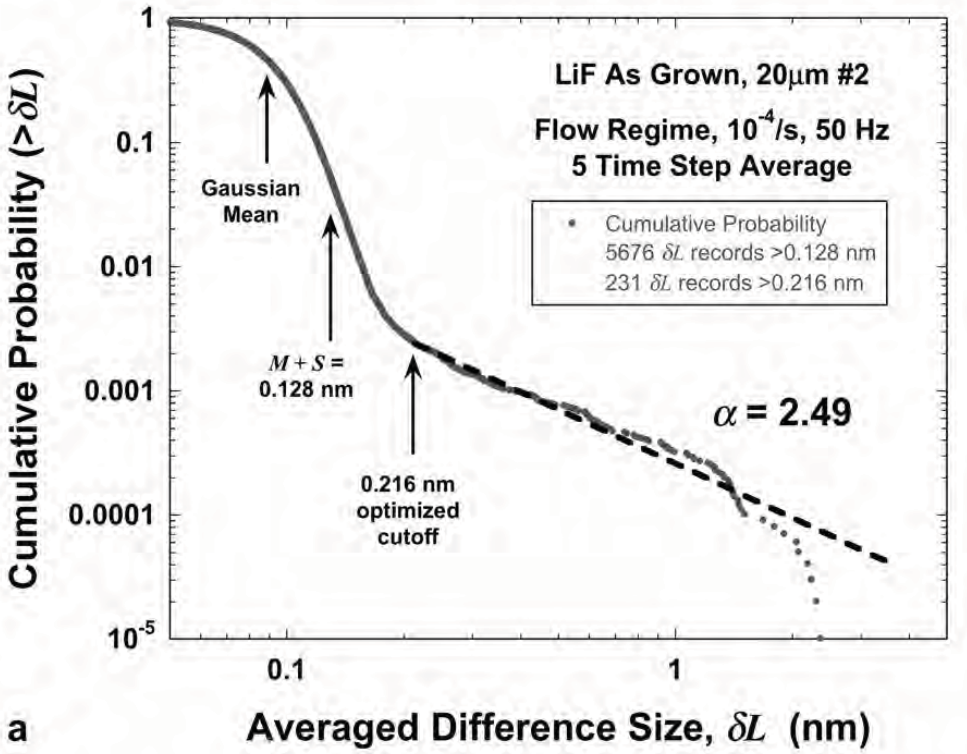
LiF As Grown, 20μm #2
Flow Regime, 10^-4/s, 50 Hz
5 Time Step Average
Cumulative Probability
5676 δL records >0.128 nm
231 δL records >0.216 nm
Gaussian Mean
M + S = 0.128 nm
0.216 nm optimized cutoff
α = 2.49
Cumulative Probability (>δL)
Averaged Difference Size, δL (nm)
a

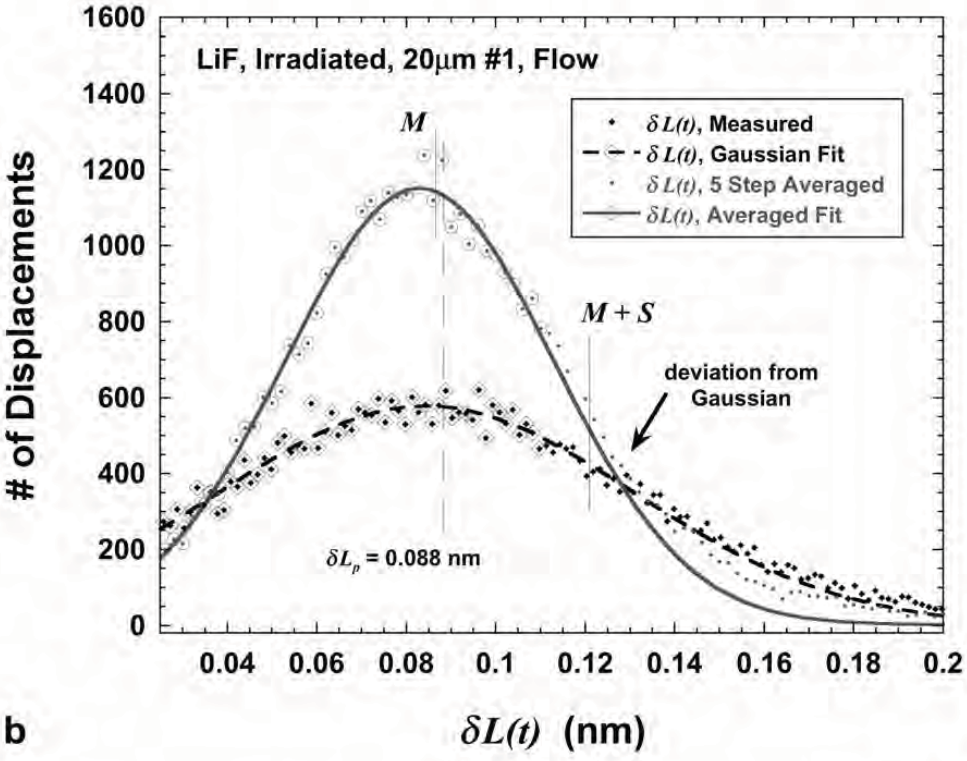
LiF, Irradiated, 20μm #1, Flow
δL(t), Measured
δL(t), Gaussian Fit
δL(t), 5 Step Averaged
δL(t), Averaged Fit
M
M + S
deviation from Gaussian
δL_p = 0.088 nm
# of Displacements
δL(t) (nm)
b

Figure 3

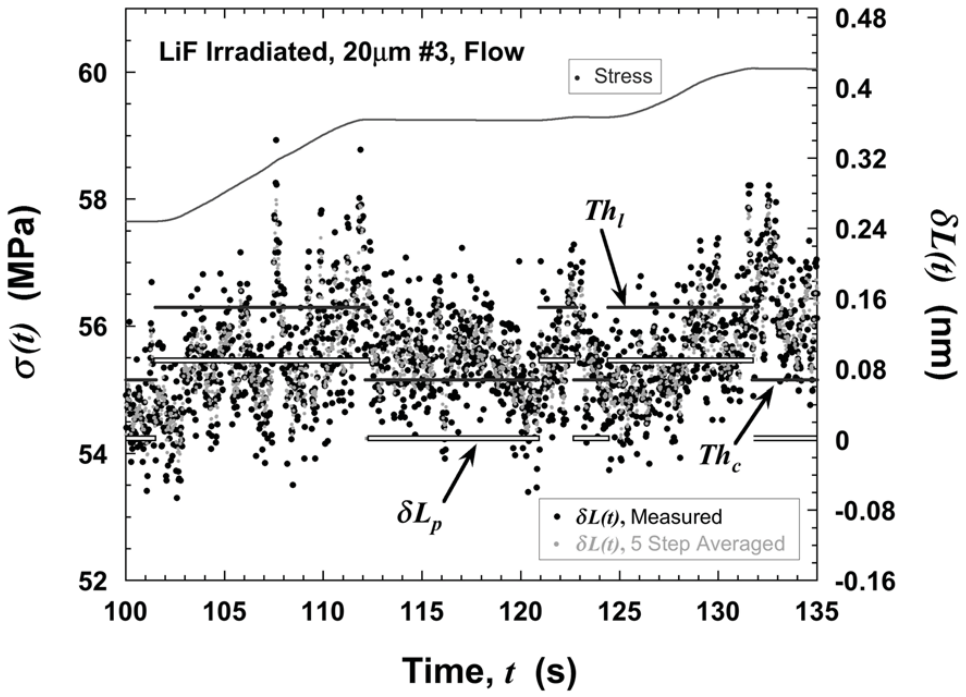
LiF Irradiated, 20μm #3, Flow
Stress
Th_l
Th_c
δL_p
$\delta L(t)$, Measured
$\delta L(t)$, 5 Step Averaged
$\sigma(t)$ (MPa)
$\delta L(t)$ (nm)
Time, t (s)
60
58
56
54
52
0.48
0.4
0.32
0.24
0.16
0.08
0
-0.08
-0.16
100
105
110
115
120
125
130
135

Figure 4

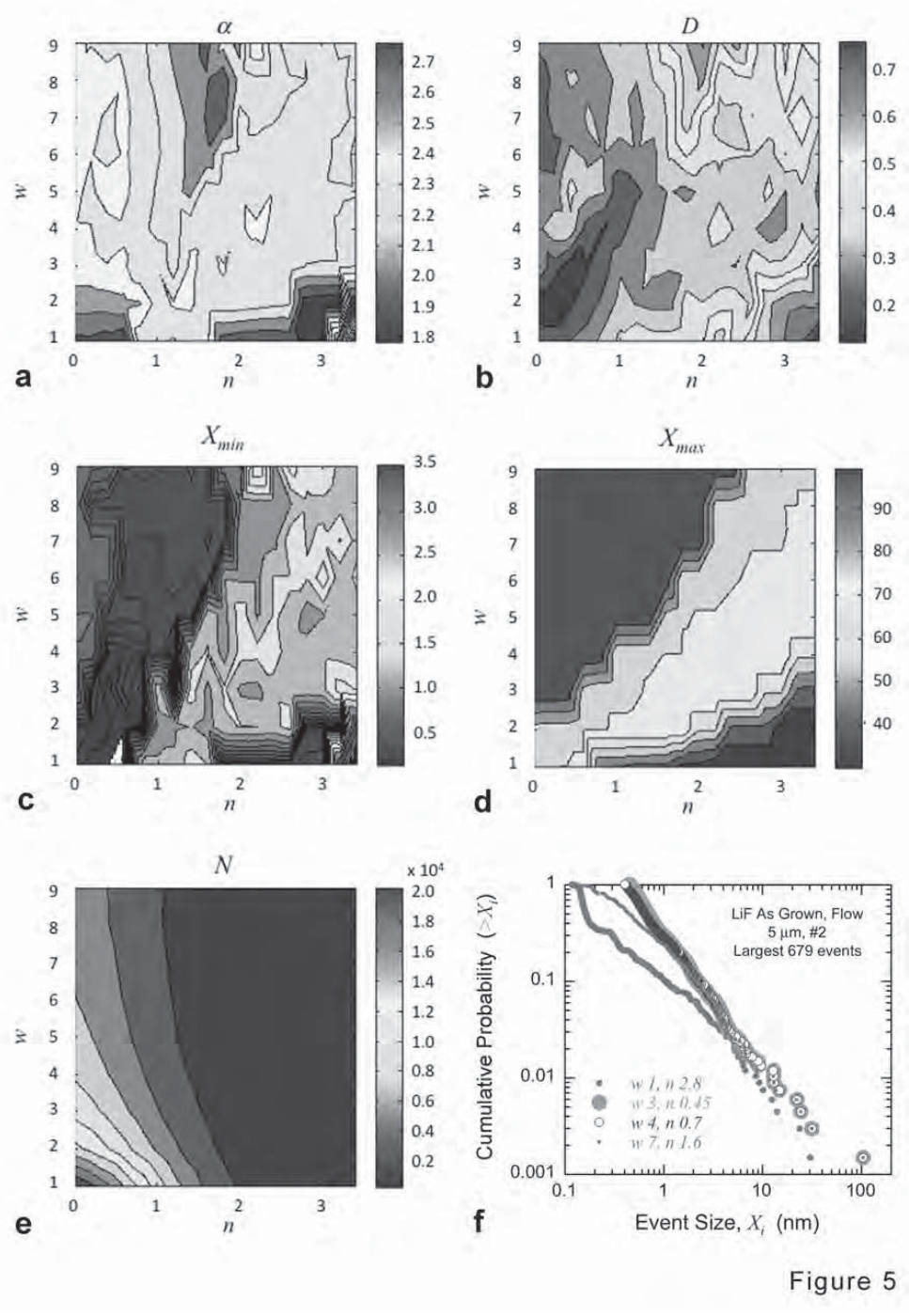
α
D
X_min
X_max
N
x 10^4
w
n
a
b
c
d
e
f
Cumulative Probability (>X_i)
Event Size, X_i (nm)
LiF As Grown, Flow
5 µm, #2
Largest 679 events
w 1, n 2.8
w 3, n 0.45
w 4, n 0.7
w 7, n 1.6

Figure 5

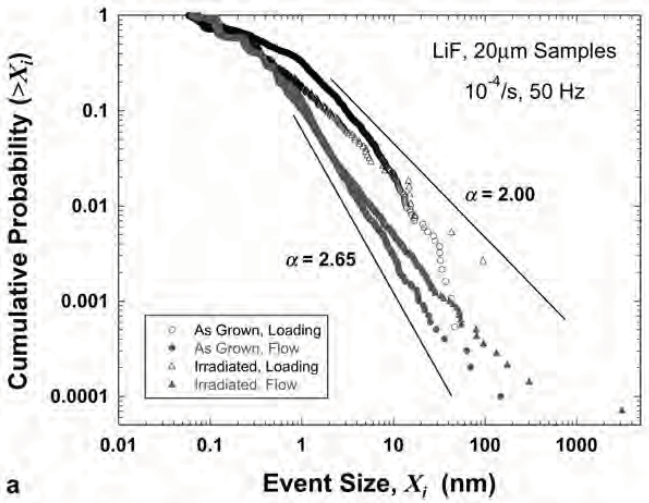
LiF, 20μm Samples
10^-4/s, 50 Hz
α = 2.00
α = 2.65
As Grown, Loading
As Grown, Flow
Irradiated, Loading
Irradiated, Flow
Cumulative Probability (>X_i)
Event Size, X_i (nm)
a

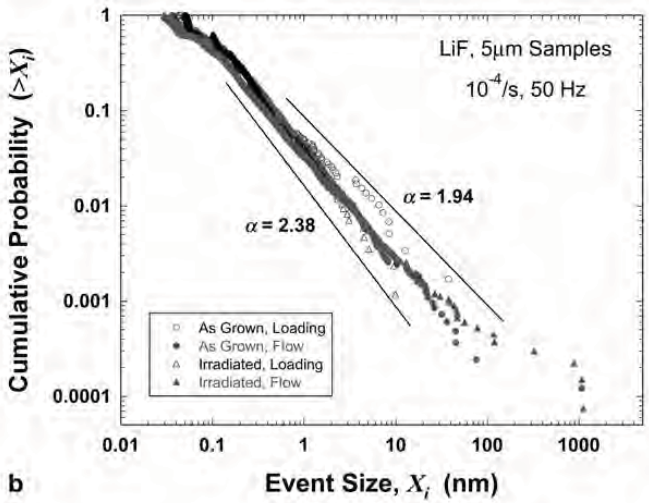
LiF, 5μm Samples
10^-4/s, 50 Hz
α = 1.94
α = 2.38
As Grown, Loading
As Grown, Flow
Irradiated, Loading
Irradiated, Flow
Cumulative Probability (>X_i)
Event Size, X_i (nm)
b

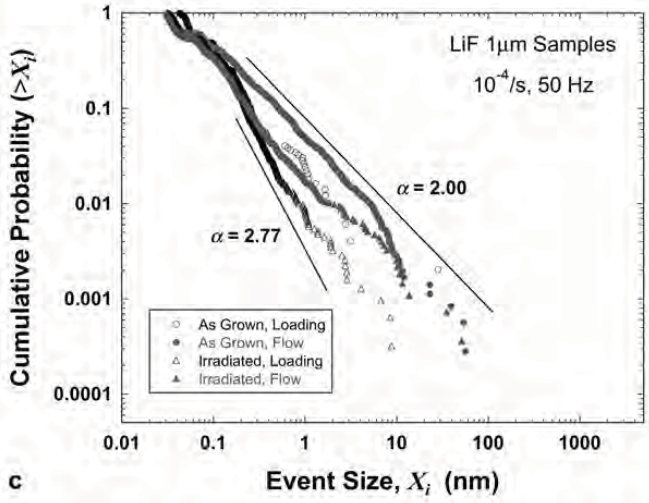
LiF 1μm Samples
10^-4/s, 50 Hz
α = 2.00
α = 2.77
As Grown, Loading
As Grown, Flow
Irradiated, Loading
Irradiated, Flow
Cumulative Probability (>X_i)
Event Size, X_i (nm)
c

Figure 6

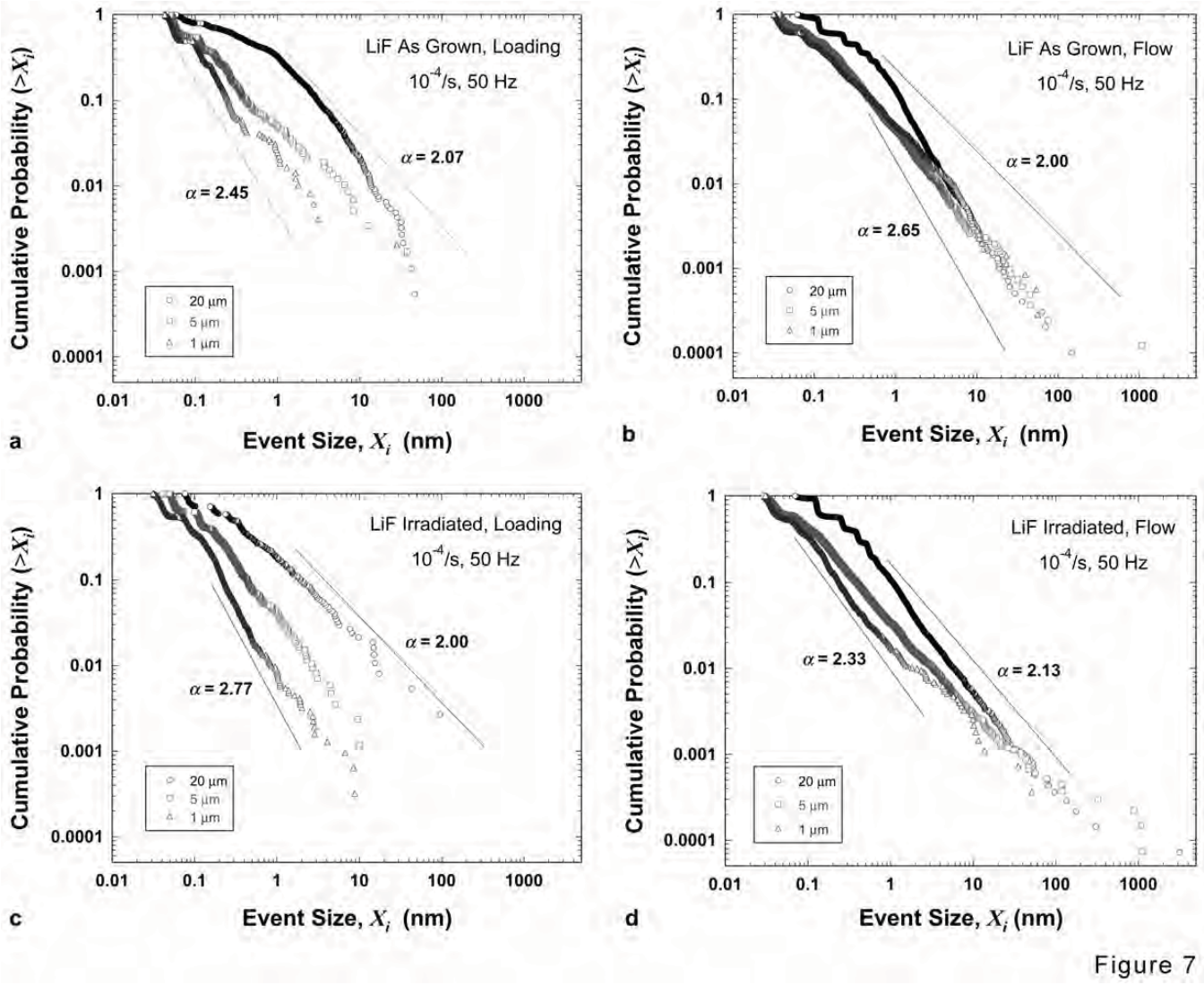
LiF As Grown, Loading
10^-4/s, 50 Hz
α = 2.45
α = 2.07
20 μm
5 μm
1 μm
Cumulative Probability (>X_i)
Event Size, X_i (nm)
a
LiF As Grown, Flow
10^-4/s, 50 Hz
α = 2.65
α = 2.00
b
LiF Irradiated, Loading
10^-4/s, 50 Hz
α = 2.77
α = 2.00
c
LiF Irradiated, Flow
10^-4/s, 50 Hz
α = 2.33
α = 2.13
d

Figure 7

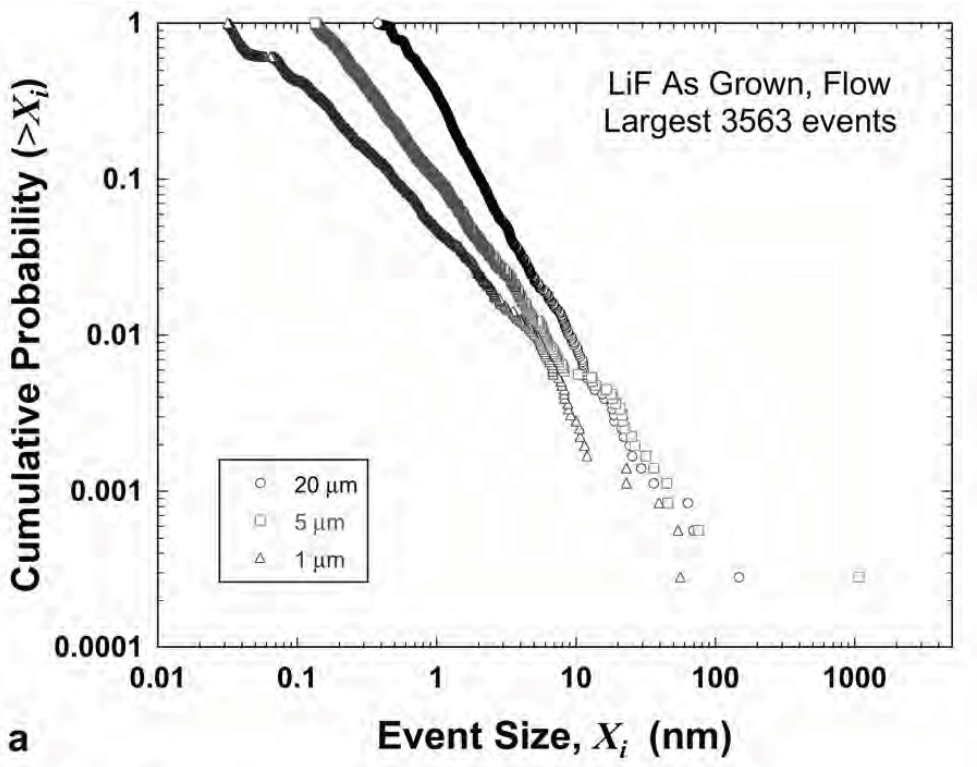
LiF As Grown, Flow
Largest 3563 events
20 μm
5 μm
1 μm
Cumulative Probability (>X_i)
Event Size, X_i (nm)
1
0.1
0.01
0.001
0.0001
0.01
0.1
1
10
100
1000

a

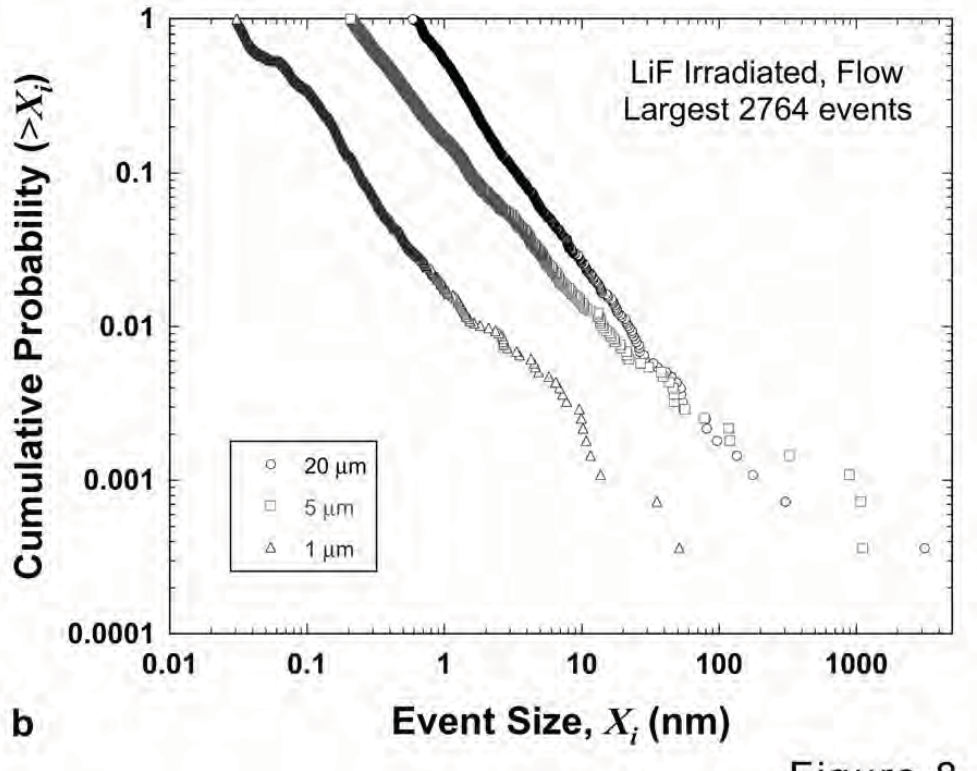
LiF Irradiated, Flow
Largest 2764 events
20 μm
5 μm
1 μm
Cumulative Probability (>X_i)
Event Size, X_i (nm)
1
0.1
0.01
0.001
0.0001
0.01
0.1
1
10
100
1000

b

Figure 8

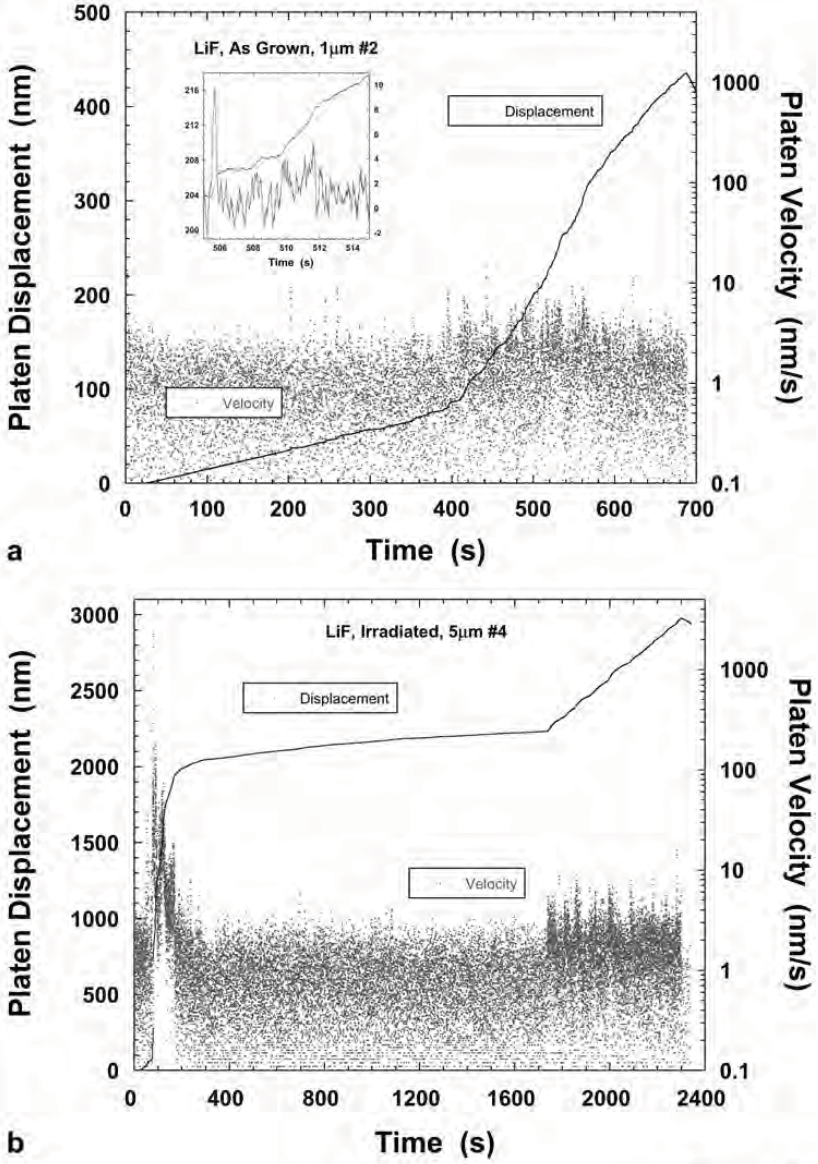
LiF, As Grown, 1μm #2
Displacement
Velocity
Platen Displacement (nm)
Platen Velocity (nm/s)
Time (s)
a
LiF, Irradiated, 5μm #4
Displacement
Velocity
Platen Displacement (nm)
Platen Velocity (nm/s)
Time (s)
b

Figure 9

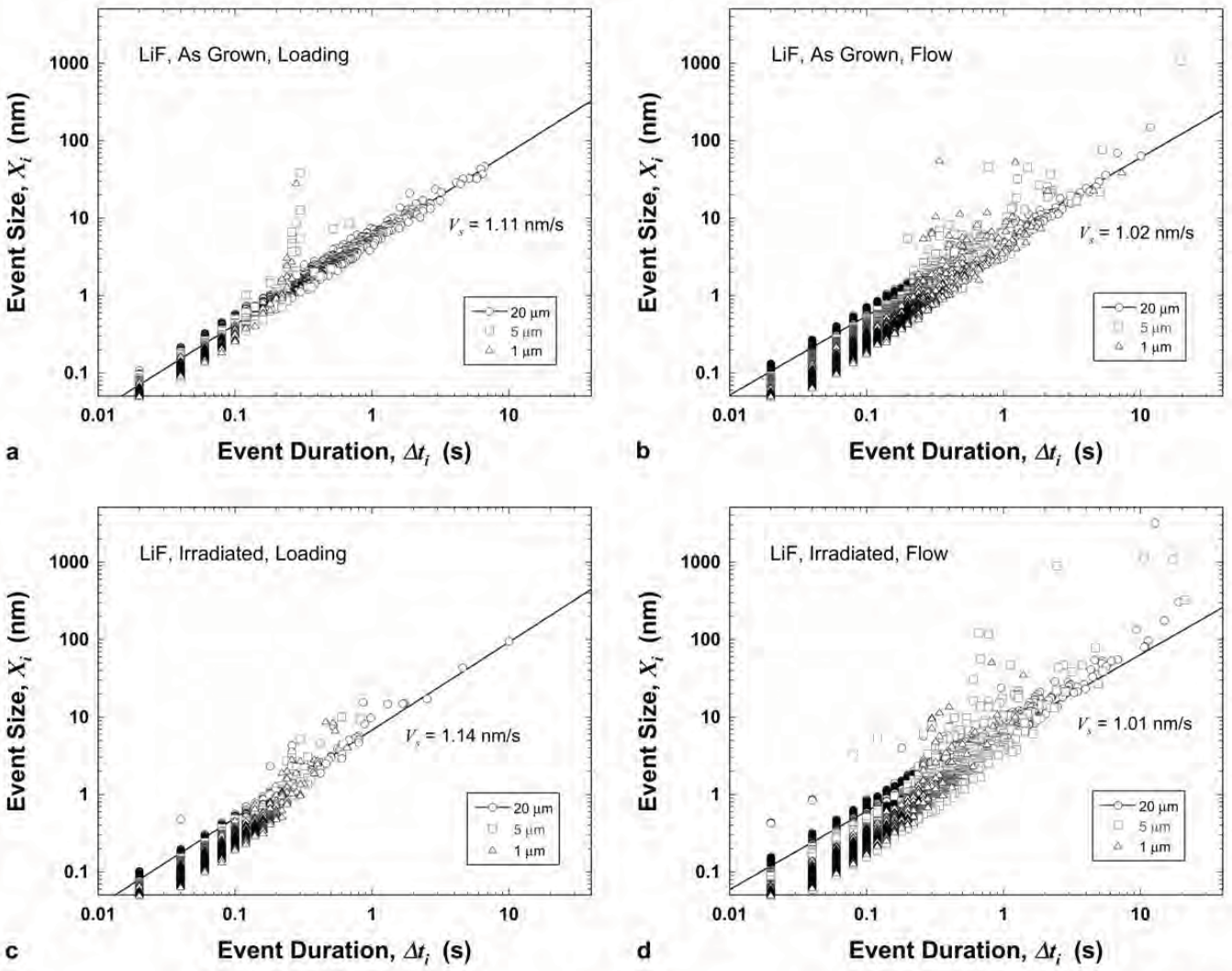
LiF, As Grown, Loading
V_s = 1.11 nm/s
20 μm
5 μm
1 μm
Event Size, X_i (nm)
Event Duration, Δt_i (s)
a
LiF, As Grown, Flow
V_s = 1.02 nm/s
b
LiF, Irradiated, Loading
V_s = 1.14 nm/s
c
LiF, Irradiated, Flow
V_s = 1.01 nm/s
d

Figure 10

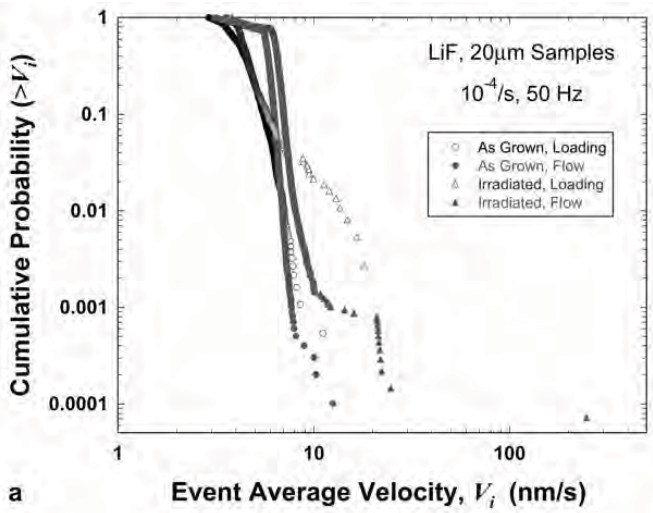

a

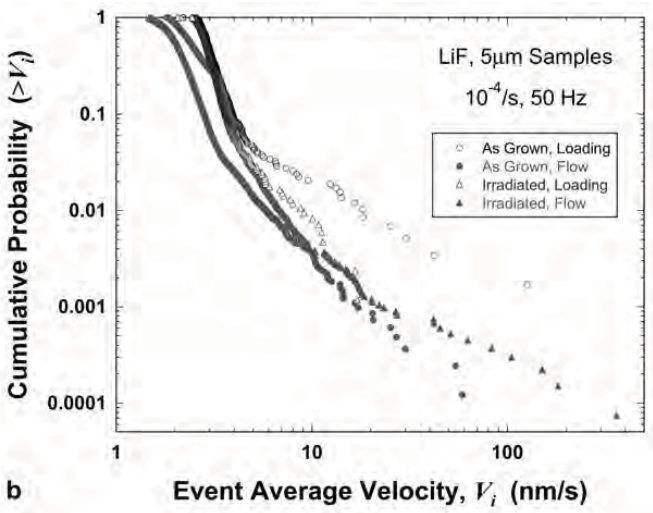

b

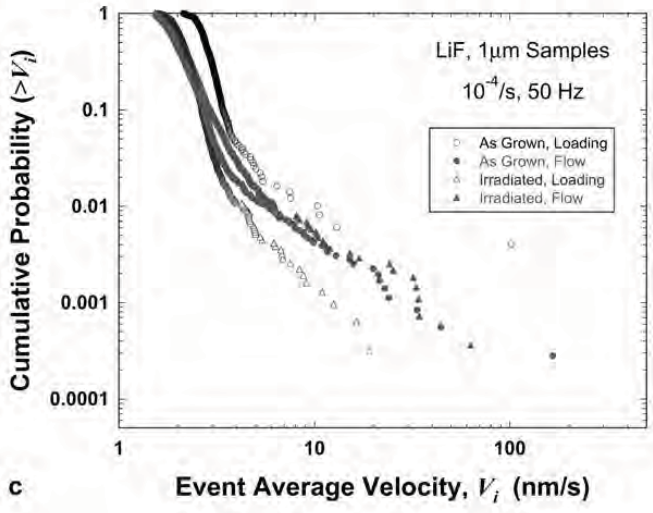

c

Figure 11

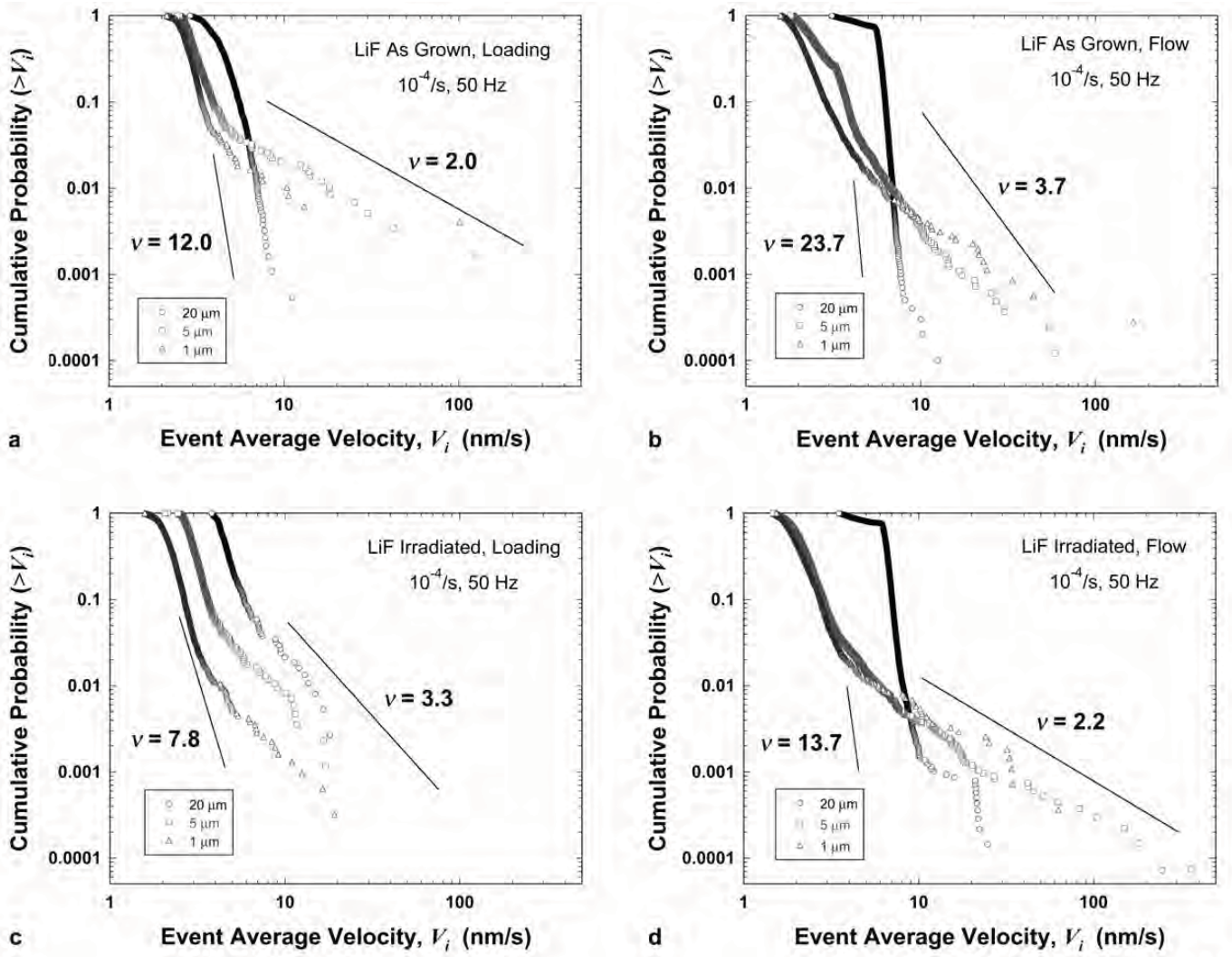
LiF As Grown, Loading
10^-4/s, 50 Hz
ν = 2.0
ν = 12.0
20 μm
5 μm
1 μm
Cumulative Probability (>V_i)
Event Average Velocity, V_i (nm/s)
a
LiF As Grown, Flow
10^-4/s, 50 Hz
ν = 3.7
ν = 23.7
b
LiF Irradiated, Loading
10^-4/s, 50 Hz
ν = 3.3
ν = 7.8
c
LiF Irradiated, Flow
10^-4/s, 50 Hz
ν = 2.2
ν = 13.7
d

Figure 12

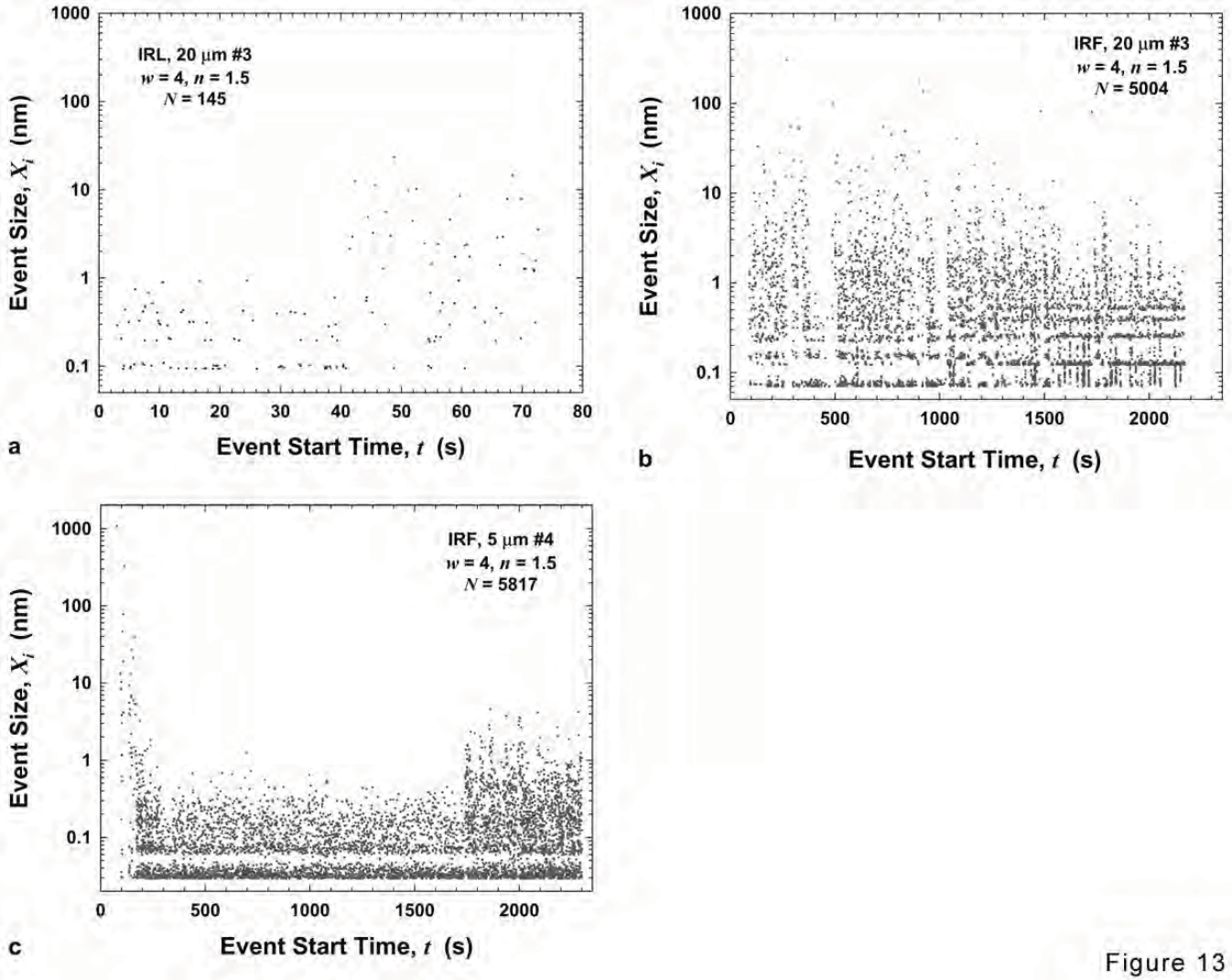
IRL, 20 μm #3
w = 4, n = 1.5
N = 145
Event Size, X_i (nm)
Event Start Time, t (s)
a
IRF, 20 μm #3
w = 4, n = 1.5
N = 5004
Event Size, X_i (nm)
Event Start Time, t (s)
b
IRF, 5 μm #4
w = 4, n = 1.5
N = 5817
Event Size, X_i (nm)
Event Start Time, t (s)
c

Figure 13

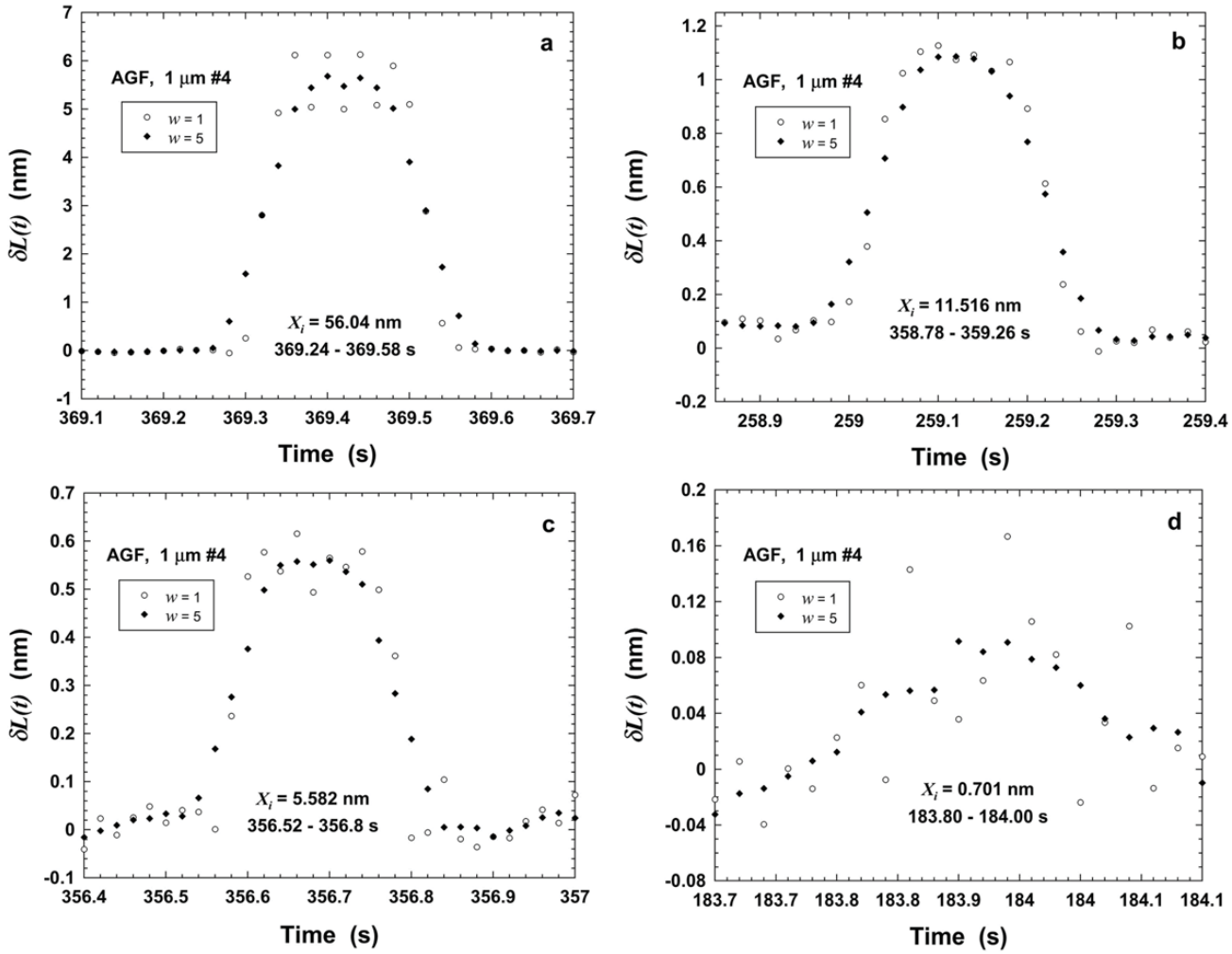
a
AGF, 1 μm #4
w = 1
w = 5
X_i = 56.04 nm
369.24 - 369.58 s
δL(t) (nm)
Time (s)
b
AGF, 1 μm #4
w = 1
w = 5
X_i = 11.516 nm
358.78 - 359.26 s
δL(t) (nm)
Time (s)
c
AGF, 1 μm #4
w = 1
w = 5
X_i = 5.582 nm
356.52 - 356.8 s
δL(t) (nm)
Time (s)
d
AGF, 1 μm #4
w = 1
w = 5
X_i = 0.701 nm
183.80 - 184.00 s
δL(t) (nm)
Time (s)

Figure 14

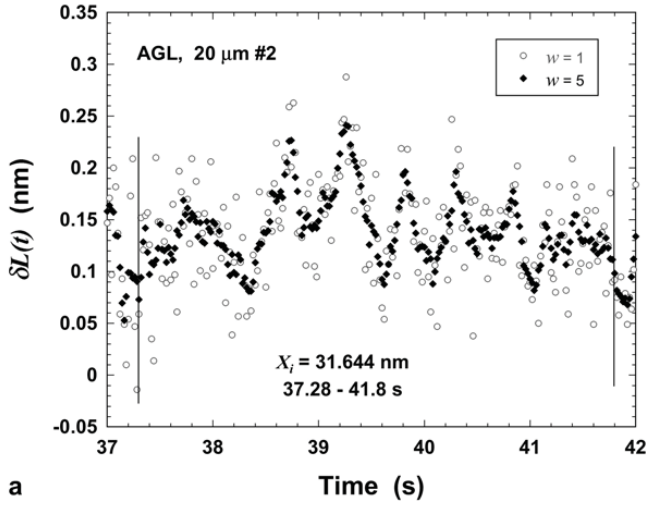
AGL, 20 μm #2
w = 1
w = 5
δL(t) (nm)
X_i = 31.644 nm
37.28 - 41.8 s
Time (s)

a

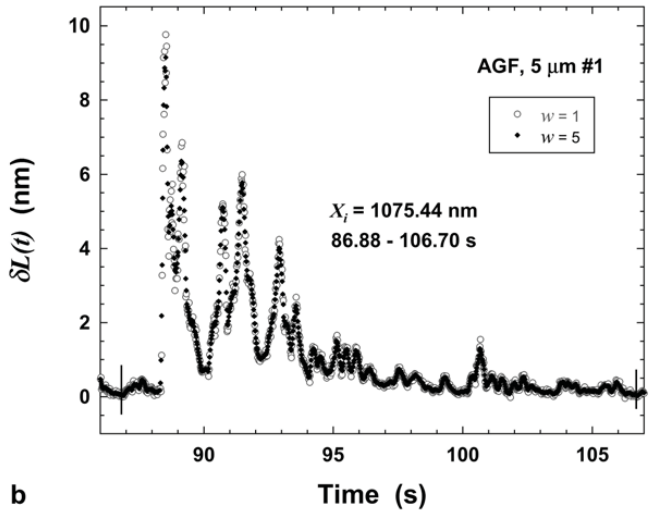
AGF, 5 μm #1
w = 1
w = 5
δL(t) (nm)
X_i = 1075.44 nm
86.88 - 106.70 s
Time (s)

b

Figure 15